Delft University of Technology

MSc thesis report

Radio Resource Management for Joint Communication and Sensing (JCAS) Services in 6G Networks

Author:

Giacomo Mazzola

Supervisors:

Dr. Remco Litjens MSc
Associate Professor, TU Delft & Senior Scientist, TNO

Dr. Kallol Das
Senior Scientist, TNO

Prof. Dr. Haibin Zhang
Professor, National Taiwan University & Senior Scientist, TNO

October 4, 2024

Abstract

This thesis explores Radio Resource Management (RRM) techniques for Joint Communication and Sensing (JCAS) in beyond-5G/6G networks. JCAS integrates communication and sensing functionalities into a unified network, promising enhanced spectral efficiency, reduced system costs, and improved performance in various applications such as autonomous vehicles and smart cities. However, efficiently managing the dual requirements of communication and sensing in a shared network is a significant challenge, especially in dense, multi-cell environments.

The work presents a novel approach to JCAS by developing advanced resource management algorithms aimed at optimizing communication throughput and sensing accuracy, with a focus on target detection as the primary sensing task. The proposed algorithms encompass topology selection, dynamic node contribution management, and joint scheduling of sensing and communication tasks. Through extensive simulations, we analyze the trade-offs between communication and sensing performance, considering metrics such as the average and 10^{th} percentile user throughput and probability of detection. The results demonstrate the effectiveness of the proposed strategies in managing interference and improving system performance in a cooperative multi-cell JCAS network.

This study contributes to the growing body of research on JCAS by addressing key limitations in existing works, such as the lack of cooperative sensing and the need for real-time dynamic resource allocation algorithms. The findings provide practical insights for network operators and lay the groundwork for future research into more complex JCAS applications and further optimization of resource management techniques.

List of Acronyms

3GPP Third Generation Partnership Project

AG Antenna Gain

ASE Area Spectral Efficiency

BS Base Station

CF Correction Factor

CRB Cramer-Rao Bound

CSI Channel State Information

CoMP Coordinated Multi-Point

DDRB Delay Doppler Resource Block

DFRC Dual-Function(al) Radar Communications

ISAC Integrated Sensing and Communication

ISD Inter-Site Distance

IoT Internet of Things

JCAS Joint Communication and Sensing

JRC Joint Radar and Communication

KPI Key Performance Indicator

LoS Line of Sight

MCL Minimum Coupling Loss

MCS Modulation and Coding Scheme

MIESM Mutual Information Effective SINR Mapping

MISO Multiple-Input Single-Output

MRC Maximum Ratio Combining

MRT Maximum Ratio Transmission

MU-MIMO Multi-User Multiple-Input Multiple-Output

NLoS Non Line of Sight

OFDM Orthogonal Frequency Division Multiplexing

OTFS Orthogonal Time Frequency Space

PF Proportional Fair

PL Path Loss

PMN Perceptive Mobile Network

PRB Physical Resource Block

Pd Probability of Detection

Pfa Probability of False Alarm

QAM Quadrature Amplitude Modulation

QoS Quality of Service

RadCom Radar Communications

RCS Radar Cross Section

RRM Radio Resource Management

SINR Signal-to-Interference-plus-Noise Ratio

SNR Signal-to-Noise Ratio

SSB Synchronization Signal Blocks

SU-MIMO Single-User Multiple-Input Multiple-Output

TTI Transmission Time Interval

UE User Equipment

UMa Urban Macro

ZF Zero Forcing

List of Figures

Contents

Chapter 1

Introduction

This chapter provides essential background knowledge on Joint Communication and Sensing (JCAS) networks, with a particular focus on introducing sensing concepts for readers more familiar with the communications domain. It also outlines the objectives of this thesis, presents an overview of the thesis structure, and introduces the notation used throughout the document.

1.1 JCAS

Joint Communication and Sensing (JCAS) is an emerging feature envisioned for future beyond-5G/6G networks, representing a paradigm shift in wireless systems design. The driving force behind JCAS lies in the growing need for enhanced network capabilities, including high data rates, low latency, and improved spectral efficiency, coupled with the increasing demand for precise sensing and localization in diverse applications such as autonomous vehicles, industrial automation, and smart cities. As the wireless spectrum becomes increasingly congested, integrating communication and sensing functionalities into a single system allows for more efficient use of available resources. This integrated approach is addressed in the literature also as Perceptive Mobile Network (PMN) [1], Integrated Sensing and Communication (ISAC) [2], Joint Radar and Communication (JRC) [3], Radar Communications (RadCom) [4], Dual-Function(al) Radar Communications (DFRC) [5] and JCAS [6]. In this work, we adopt the latter term.

JCAS represents an advanced integration of communication and radar systems, which can be implemented at different levels. This integration ranges from simple coexistence, where systems operate independently and may interfere with each other, to complete convergence, where systems share hardware, waveforms, and resources such as frequency bands and power [7]. There are three primary approaches to integrating communication and radar systems: communication-centric, radar-centric, and joint-designed systems. The communication-centric approach introduces sensing capabilities into an existing communication network. Conversely, the sensing-centric approach adds communication capabilities to an existing radar system. Joint-designed systems are developed from the ground up to balance the trade-offs between communication and sensing, resulting in a system that inherently supports both functions.

The benefits of JCAS extend beyond resource efficiency. First, *integration gains* arise from the shared use of hardware and spectrum, reducing system costs, spectral needs and energy consumption. Second, *coordination gains* result from the improved coexistence of communication and sensing functions, as interference between them can be minimized or even leveraged to enhance performance, by using sensing signals to improve channel estimation or mobility management in communication flows or by opportunistically using communication-oriented signals to enhance sensing performance [8]. Several key use cases motivate the introduction of JCAS in 6G networks. These include enhanced automotive radar systems for autonomous driving, where integrated communication and sensing can improve safety and navigation; smart cities, where sensor networks and communication infrastructure can be seamlessly combined to monitor and manage urban environments; and industrial Internet of Things (IoT), where precise sensing and robust communication are critical for automation and control. These applications underscore the potential of JCAS to revolutionize the next generation of mobile networks, providing both economic and technological benefits.

1.2 Sensing and radar systems

Sensing encompasses a variety of tasks, including detection, localization, surveillance, and tracking, which are typically performed by radar systems. Each of these tasks has specific requirements:

- **Detection** involves identifying the presence of objects or events within a specified area, requiring high sensitivity and accuracy to minimize false alarms and missed detections.
- **Localization** determines the precise position of detected objects, which demands accurate distance and angle measurements to ensure reliability.
- **Surveillance** involves monitoring an area for prolonged periods to gather comprehensive data on activities and changes, requiring sustained performance and the ability to process large volumes of data efficiently.
- **Tracking** follows the movement of objects over time, necessitating consistent updates and robust algorithms to handle dynamic environments and maintain continuous observation.

Radar (Radio Detection and Ranging) systems perform various sensing tasks by emitting electromagnetic waves and analyzing the reflections, or "echoes", from objects in the environment. These echoes provide information about the presence, location, and movement of objects, which the radar system processes to accomplish its sensing objectives.

Depending on how the transmitters and receivers are spatially arranged, radar systems can be configured as *monostatic*, *bistatic*, or *multistatic* sensing systems. These configurations, illustrated in Figure 1.1, offer distinct advantages for different sensing applications and are defined as follows:

1. **Monostatic Sensing:** In this configuration, the transmitter and receiver are co-located, typically within the same device. The radar system transmits a signal and uses the same unit to receive the reflected echoes from objects. Monostatic radar systems are widely favored for their simplicity and compactness, making them ideal for applications such as automotive sensing, weather monitoring, and air traffic control.
2. **Bistatic Sensing:** This setup involves separate locations for the transmitter and receiver. The spatial separation allows radar systems to cover areas that might be inaccessible to monostatic configurations and reduces interference from the transmitter at the receiver. Bistatic radar systems are advantageous in scenarios requiring stealth or long-range detection. However, they necessitate more complex implementations due to the need for precise synchronization between the transmitter and receiver.
3. **Multistatic Sensing:** In multistatic configurations, multiple transmitters and receivers are positioned at different locations. This arrangement enhances spatial coverage and detection reliability

by collecting signals from various perspectives, thereby improving the accuracy of tasks such as localization and tracking. Multistatic radar systems are particularly beneficial in complex environments where redundancy and multi-angle observations are critical.

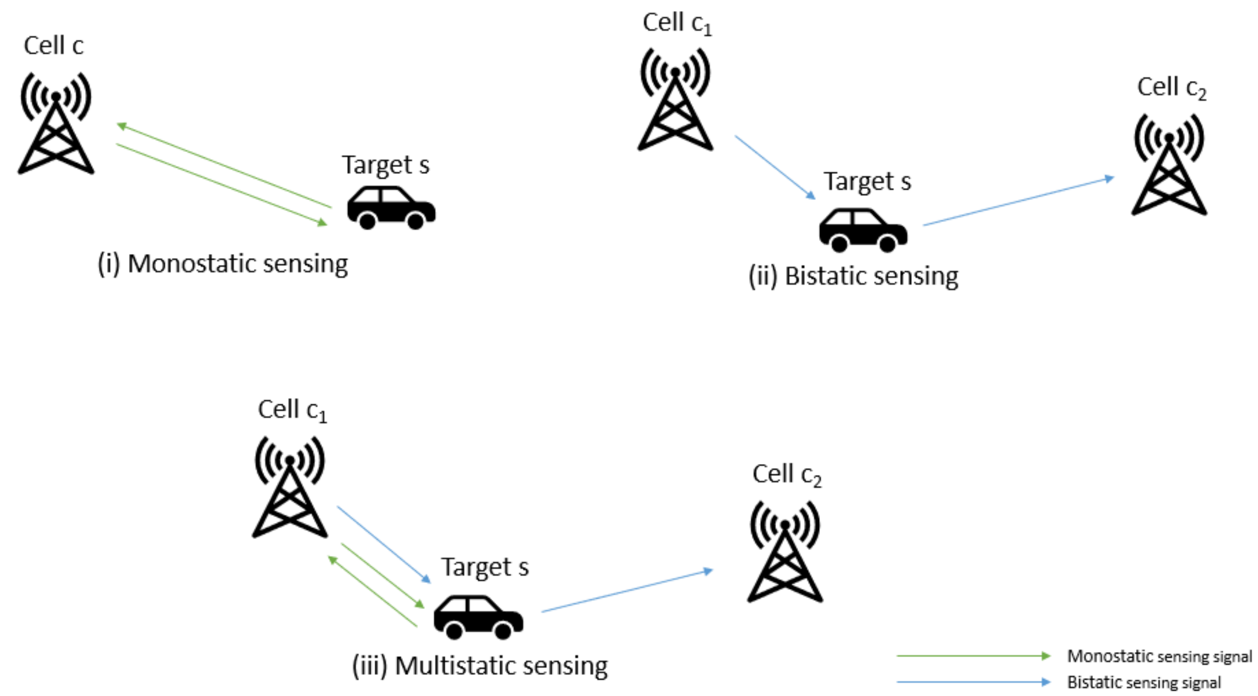

Figure 1.1: Three main configurations of a sensing radar system: (i) monostatic, (ii) bistatic and (iii) multistatic.

1.3 Scope and objective

The focus of our thesis is on radio resource management in communication-centric JCAS networks, specifically within a beyond-5G/6G mobile network, and we limit our analysis to target detection, leaving other sensing tasks as future work. The objective of this thesis is to develop a novel JCAS network model and propose resource management algorithms, aimed at improving both communication and sensing performance. These algorithms are evaluated across a range of scenarios, with the goal of understanding their impact on system performance and optimizing the trade-off between sensing and communication.

Our work concentrates on cooperative JCAS networks, where a cluster of Base Stations (BSs)—and in certain cases, UEs—jointly contribute to the sensing task. The proposed topology management scheme dynamically selects the optimal set of transmitters and receivers to perform detection, allowing for flexibility in using monostatic, bistatic, or multistatic configurations, depending on the context. By focusing on detection as the primary sensing task, we aim to enhance accuracy while maintaining efficient communication performance, leaving other sensing tasks for future exploration.

1.4 Thesis overview

This thesis is organized into seven chapters. In this introductory chapter, we provide background information on JCAS and outline the central objectives of the study. Chapter 2 presents a comprehensive review of related work and highlights the contributions of this research. Chapters 3 and 4 detail the key modeling aspects adopted in this work. Chapter 5 introduces the resource management solutions developed and evaluated in this thesis. Chapter 6 describes the simulated scenarios along with their respective results, followed by a discussion of the observed trends, supported by intuitive and qualitative explanations. Finally, Chapter 7 concludes with a summary of the findings and offers recommendations for future research.

1.5 Notation

The notations used in this work are as follows. Matrices are denoted by bold capital letters, such as $\mathbf{H}$. The element at the i^{th} row and j^{th} column of a matrix $\mathbf{H}$ is written as $\mathbf{H}[i, j]$, while $\mathbf{H}_j$ denotes the j^{th} column vector. The transpose, conjugate transpose, inverse, and Moore-Penrose pseudo-inverse of $\mathbf{H}$ are represented as $\mathbf{H}^T$, $\mathbf{H}^*$, $\mathbf{H}^{-1}$, and $\mathbf{H}^+$, respectively. The notation $abs(\mathbf{H})$ denotes the element-wise absolute value of the matrix $\mathbf{H}$, while $\mathbf{H}^2$ represents the element-wise square of $\mathbf{H}$. Specifically, for each entry $\mathbf{H}[i, j]$ in $\mathbf{H}$, the corresponding entry in $abs(\mathbf{H})$ is $|\mathbf{H}[i, j]|$, and in $\mathbf{H}^2$ it is $(\mathbf{H}[i, j])^2$. $\mathbf{H}(t)$ denotes the value of $\mathbf{H}$ at time t.

Vectors are represented by bold lowercase letters, such as $\mathbf{h}$. The conjugate transpose of vector $\mathbf{h}$ is written as $\mathbf{h}^*$, and $abs(\mathbf{h})$ represents the element-wise absolute value of $\mathbf{h}$. The element of vector $\mathbf{h}$ at index i is denoted as $\mathbf{h}[i]$, while $\|\mathbf{h}\|_2$ represents the L2-norm of vector $\mathbf{h}$. For a complex scalar x, $|x|$ denotes the modulus of x.

Chapter 2

Related works and contributions of this thesis

Most of the works studying radio resource management in JCAS systems focus on resource allocation at link/system level in single-cell scenarios. Significant research has been conducted on beamforming techniques [9][10][11][12], waveform optimization [13][14], power allocation [15], time/frequency multiplexing [15][16] and security [17]. Here we analyze in more detail only the works that are relevant to our study. For instance, [15] implements power allocation and spectrum partitioning algorithm to optimize the aggregated sensing and communication performance and energy efficiency of JCAS systems by using fractional and parametric programming techniques for convex problems. [16] optimizes time and frequency allocation through the innovative use of Delay Doppler Resource Block (DDRB) allocation in Orthogonal Time Frequency Space (OTFS)-based JCAS systems, optimizing the sum rate of multiple users while satisfying stringent power and Cramer-Rao Bound (CRB) constraints for enhanced communication and sensing performance.

Some work has also been done in the area of multi-cell JCAS networks. For instance, the authors in [18] develop a robust framework for optimizing resource allocation and user-cell association in a multi-cell JCAS network. Specifically, the resources managed within their model include the allocation of different sub-bands to minimize inter-cell interference, association of users to optimize network coverage and utilization, and control of transmission power to balance signal quality against energy consumption. [19] explores a power allocation method to improve localization accuracy while managing interference between base stations. It also proposes an algorithm to minimize the range estimation errors, considering the constraints on signal quality and power usage. [20] proposes a unified resource allocation framework to fairly and effectively distribute power and bandwidth, among a range of different sensing tasks. The authors focus on managing these resources to balance the Quality of Service (QoS) demands for diverse sensing applications applications (detection, tracking and surveillance), ensuring that both sensing and communication performance is maximized under the constraints of available system resources.

A common limitation of these works is the lack of cooperation between BSs, which could potentially enhance the network's overall sensing and communication performance by leveraging shared information about the environment and user activity and minimizing inter-cell interference. Cooperative JCAS networks, in which clusters of transmitting and receiving BSs work in cooperation to enhance the sensing performance, have been already introduced in the literature as future challenges, but not much work has been done yet. For instance, [21] suggests the idea to use the signals coming from neighbouring cells as contributions for bistatic sensing instead of treating them as interference. [22] provides a framework for multi-BS cooperative sensing in JCAS networks, analyzing the enabling technologies, performance metrics and JCAS signal design and optimization. While these studies focus on promoting the cooperative JCAS network paradigm, only a handful of works tackle the radio resource management challenge.

Only limited attention has been dedicated to radio resource management at a network level in a multi-cell JCAS layout. For instance, [23] develops a cooperative JCAS scheme to mitigate the inter-cell interference, which significantly enhances network-wide sensing and communication performance. The study utilizes stochastic geometry to model and optimize network parameters effectively, such as BSs density and cluster size of serving BSs to a specific user/target, demonstrating the potential of this approach to improve both the average data rate and localization accuracy across the network. However, this work is constrained by its reliance on a theoretical framework that incorporates several simplifications, which limit its applicability to real-world scenarios. For instance, it is assumed that the positions of the BSs and other network elements are modeled using a homogeneous Poisson Point Process in a two-dimensional space. In reality, the placement of BSs is typically influenced by geographical, infrastructural, and demand-based factors, all of which can significantly affect network performance and optimal configurations. [24], which is an extension of [23], also utilizes stochastic geometry for developing mathematical models that derive tractable expressions for Area Spectral Efficiency (ASE) to evaluate and optimize the performance of JCAS networks. ASE measures the spectrum efficiency over a given area for both communication and sensing tasks. By focusing on ASE, the authors aim to quantify the efficiency of spatial resource utilization and the overall performance of the network. These expressions account for factors such as inter-cell interference and the spatial distribution of base stations, users, and targets. The authors then optimize the ASE by adjusting the cooperative base station cluster sizes and the number of users and targets. For communication, ASE is maximized by optimizing spatial resources to enhance multiplexing and diversity gains, while for sensing, ASE is optimized by mitigating sensing interference through cooperative strategies like interference nulling. The combined ASE reflects the overall efficiency of the network in utilizing the spectrum for both tasks.

[25] builds upon [24] by introducing a constraint for limited backhaul capacity, which restricts the size of BS clusters. Beyond this size, BSs can no longer be considered synchronized, and such sizes are excluded from the analysis since coherent sensing cannot be performed. Additionally, [26] extends the analysis of [25] to scenarios with limited backhaul capacity, assuming non-coherent sensing processing. This work also integrates transmit power management into the algorithm, wherein the available power is allocated between spatially multiplexed sensing and communication signals. Authors in [27] develop a robust precoding framework for Multiple-Input Single-Output (MISO) multi-cell JCAS network. It introduces methods to optimize sensing performance using CRB and enhance communication SINR using and Coordinated Multi-Point (CoMP). The approach tackles channel state estimation errors and non-convex optimization challenges using advanced mathematical techniques.

The works analysed in this literature review are summarised in Table 2.1 by outlining the considered scenario, the addressed resource management challenges, the applied solution approach and the pursued performance objective each reference addresses, thus enabling us to identify possible research gaps.

The literature review reveals that most of the analyzed works employ analytical methods to optimize network parameters, such as the number of users or targets and the size of BS clusters, typically under simplified conditions. However, a common limitation among these studies is the absence of algorithms for real-time dynamic resource allocation in JCAS networks. Such algorithms are necessary

Table 2.1: Overview of related research.

Ref	Objective	Scenario	Resource Scheduling	Topology Management/Clustering	Power Allocation	Management Technique	Performance Objective
[9]	Design optimized hybrid and analog beamforming algorithm in FD JCAS systems	Single cell, multi user, single target	Space	No	Yes	Closed form and numerical approaches	Maximize power in sensing direction while limiting communication interference
[10]	Design a vision aided beamforming algorithm to compensate for user location uncertainty	Single cell, multi users	Space	No	Yes	Deep reinforcement	Maximize SINR for users
[11]	Optimize predictive beamforming in high-mobility scenarios	Single cell, single user	Time, space	No	No	Exhaustive search	Maximize user's throughput while meeting sensing performance constraint
[12]	Design optimized hybrid beamforming algorithm for FD JCAS systems	Single cell, multi users, multi targets	Space	No	Yes	Generalized Rayleigh Quotient (GRQ) and Genetic Algorithms (GA)	Maximize communication sum-rate while meeting sensing constraints
[13]	Utilize cyclic prefixed single carrier (CP-SC) waveforms in JCAS systems	-	Spectrum and waveform utilization	No	No	Fast Cyclic Correlation Radar (FCCR) and Maximum Likelihood Estimation	Estimation accuracy and computational efficiency
[14]	JCAS waveform optimization in OFDM communication-centric systems	-	Spectrum and waveform utilization	No	No	Numerical iteration algorithm	Maximize communication SINR while constraining either mutual information (MI) or Cramer-Rao bound (CRB) of sensing
[15]	Develop a joint spectrum partitioning (SP) and power allocation (PA) optimization framework	Single cell	Frequency	No	Yes	Solve convex optimization problem	Maximize sensing and communication performance under system constraints
[16]	Optimize resource allocation in OTFS-based ISAC systems	Single cell multi user	Time, frequency	No	Yes	Solve convex optimization problem	Maximize data rates and minimize CRB under power budget constraints
[17]	Design resource allocation framework for variable-length snapshots and injection of artificial noise (AF)	Single cell, multi users, multi targets	Space, covariance matrix of AF	No	No	Block coordinate descent and semidefinite relaxation methods	Maximize the system's sum secrecy rate while ensuring minimal information leakage and minimum average rate for each user
[18]	Design a resource allocation framework to optimize sub-band, user and power allocation	Multi cell, multi users, multi targets	Frequency, user association	No	Yes	Greedy Genetic Algorithm (GGA) Hungarian Algorithm and Successive Convex Approximation (SCA)	Maximize SINRs while meeting power constraints
[19]	Design a power allocation method that minimizes the maximum range estimate error across BSs	Multi cell, single user, single target	-	No	Yes	Convex relaxation, iterative algorithm	Minimization of the maximum std of range estimates across all BSs meeting SINR and power constraints
[20]	Define and quantify the QoS for sensing in various applications and design resource allocation framework	Single cell, multi user, multi target	Frequency	No	Yes	Alternative optimization methods	Maximize sensing QoS and communication SINR
[22]	Develop a cooperative sensing framework involving multiple BSs	Multi cell, multi user, multi target	Frequency	Cooperative BSs cluster size	Yes	Cooperative sensing algorithms	Maximize sensing accuracy and range and communication throughput and reliability
[23]–[26]	Analyze and optimize the S&C performance in JCAS networks using multi-point coordinated joint transmission (CoMP)	Multi cell, multi user, multi target	Cooperative BSs cluster size	No	No	Stochastic geometry, exhaustive search	Minimize CRLB and maximize ASE while meeting backhaul capacity constraints
[27]	Develop robust precoding for a cooperative MISO JCAS system	Multi cell, multi users, multi targets	Space	No	Yes	Semidefinite relaxation (SDR) and alternating optimization (AO) techniques	Minimize the estimation error variance of target parameters and maximize the communication SINR

to handle the scheduling of communication and sensing signals while considering time- and frequency-varying channels in real-world scenarios. Furthermore, to the best of our knowledge, no previous work has addressed the problem of sensing topology selection, which involves assigning transmitters and receivers to jointly perform sensing tasks in realistic scenarios, rather than simply optimizing cluster size in generalized settings. In response to this research gap, the contributions of this thesis are as follows:

- Develop an advanced model for a communication-centric JCAS network, that considers realistic propagation channels and interference between communication and sensing tasks, in contrast to many existing works that assume these factors to be constant or absent or assume static channel conditions [18][20][26][28].
- Design a topology selection algorithm for cooperative sensing tasks. In other words, determine the optimal configuration of transmitters and receivers for each target, balancing the need to maximize detection performance while efficiently utilizing the available node resources. In our work, we do not only consider BSs as sensing receivers, but we also extended the model to allow UEs to perform this role.
- Extend a commonly used time and space multiplexing communication user scheduling algorithm to jointly schedule sensing tasks alongside communication flows, ensuring efficient resource allocation for both functions.
- Analyze the communication and sensing trade-off based on probability of detection, communication throughput performance and the sensing topology size, through extensive simulations of a range of relevant scenarios.
- Derive insightful conclusions and, based on these findings, provide practical recommendations for network operators on how to optimally manage radio resources in JCAS networks.

Chapter 3

Modeling

In this chapter we introduce the key modeling design choices adopted in this work. Most of the communications-oriented aspects are modeled as in [29] with some modifications to extend them to a JCAS scenario.

3.1 Network modeling

In this work we use a multi-cell network layout as can be seen in Figure 3.1. The network is composed by a total of nineteen cells, served by nine three-sectorized base stations deployed according to an hexagonal layout. The Inter-Site Distance (ISD) is 500 meters which results in a cell range of about 333 meters, modeling a dense urban deployment network [30]. The height of each BS is fixed at 25 meters [30]. The cells use Orthogonal Frequency Division Multiplexing (OFDM) signals on a dedicated 20 MHz carrier in the 7.1875 GHz band configured with numerology 1 (30 kHz sub-carrier spacing). This results in a Transmission Time Interval (TTI) of 0.5 ms, where a TTI denotes the duration of transmission on the radio link. Since twelve sub-carriers make up a Physical Resource Block (PRB), each cell has $n_{prb} = 51$ PRBs [31]. The set of all PRBs is denoted as $\mathcal{F}$. The total transmit power per cell is $P_{max} = 120$ W, while the total transmit power per PRB is $\frac{P_{max}}{n_{prb}}$.

In this work, we refer to the green inner cells as "evaluation" cells, meaning that these are the cells of interest when evaluating the performance of communication and sensing tasks. On the other hand, we refer to the red outer cells as "background" cells, for which we do not simulate concrete communication or sensing tasks, but they are assumed to always radiate at a fixed power to generate inter-cell interference for the evaluation cells. Throughout the document, we will index the evaluation cells from zero to six, while the background cells will be indexed from seven to eighteen.

Finally, the UEs and the sensing targets are distributed uniformly in the area served by the evaluation cells and they are considered to be outdoor. In this work, we detenote UEs and sensing targets generally as "entities".

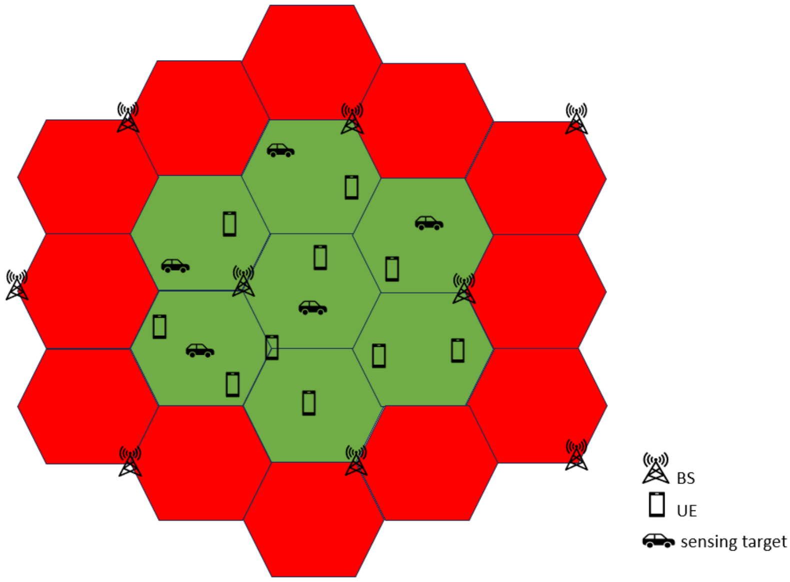

Figure 3.1: Layout of the multi-cell network adopted in this work.

3.2 Antenna modeling

Each cell is served by a 64T64R antenna array, consisting of eight rows and four columns of cross-polarized antenna elements, as shown in Figure 3.2i. This configuration results in $n_c = 64$ transmit/receive antennas. There are no sub-arrays, so the precoder for beamforming is optimized for all 64 antenna elements. The antenna gain of each antenna element is modeled as specified in the Table 7.3-1 of the Third Generation Partnership Project (3GPP) technical report TR38.901 [30], with a maximum directional gain of 8 dBi per element. The spacing between adjacent antenna elements is $\lambda/2$.

Each UE is assumed to have two pairs of cross-polarized antenna elements placed in opposite corners of the terminal, as shown in Figure 3.2ii. This configuration results in $n_{UE} = 4$ antennas. The antenna gain of all UE antenna elements is assumed to be 0 dBi. Considering the UE antenna height $h_{UE} = 1.5\ m$, the BS antenna height, and the ISD, the mechanical downward tilt for the cells is derived to be 5 degrees. The tilt is calculated by determining the angle, in degrees, that directs the antenna towards the cell edge and then rounding it down to the nearest integer, as it is common practice to aim the tilt slightly before the cell edge. Note that an appropriately configured downward tilt ensures coverage for cell edge users in the absence of shadowing and multipath fading and reduces interference for users in outer cells.

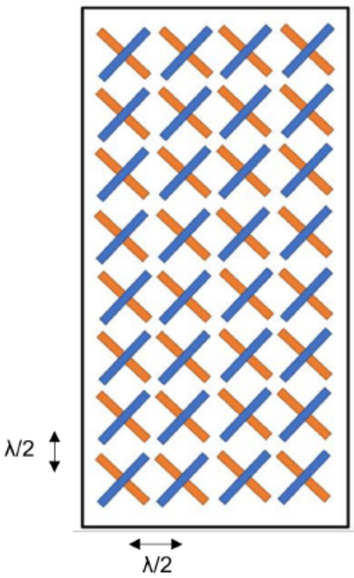

(i) BS antenna array.

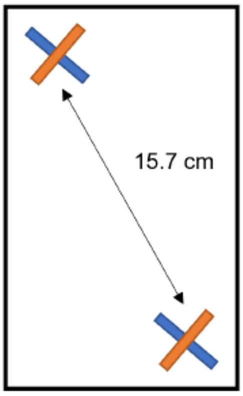

(ii) UE antenna array.

Figure 3.2: (i) Antenna array deployed at a site with half-wavelength horizontal and vertical spacing between adjacent antenna elements (ii) Antenna placement at a user terminal.

As mentioned in the previous section, the evaluation cells are modeled differently than the background cells. This difference is modeled in the antenna radiation patterns. The horizontal and vertical cut of the antenna radiation pattern of a single antenna element of an evaluation cell is shown in Figure 3.3 while the one for the background cells is shown in Figure 3.4 as depicted in [32].

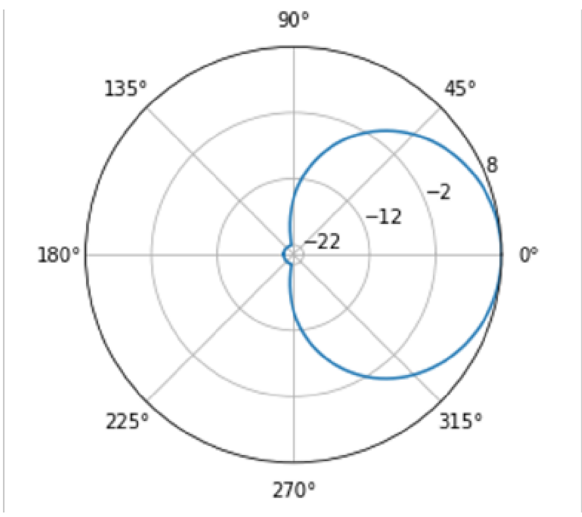

(i) Horizontal antenna gain [dB].

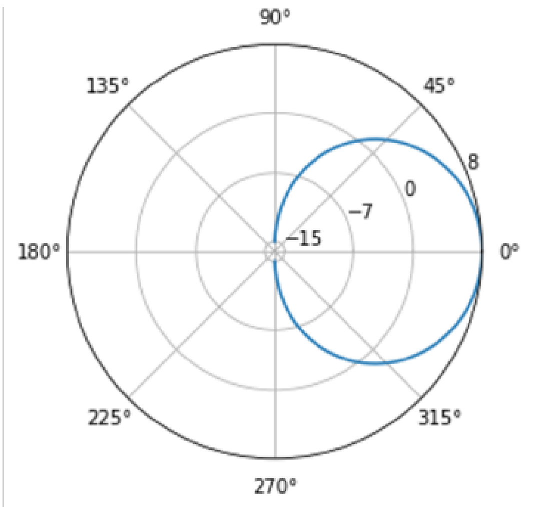

(ii) Vertical antenna gain [dB].

Figure 3.3: Horizontal and vertical antenna gains for an evaluation cell.

The sensing targets, which are objects in the environment, do not have any antennas. However, for simulation purposes, we model them as omni-directional antenna elements, as explained in Section 3.3.

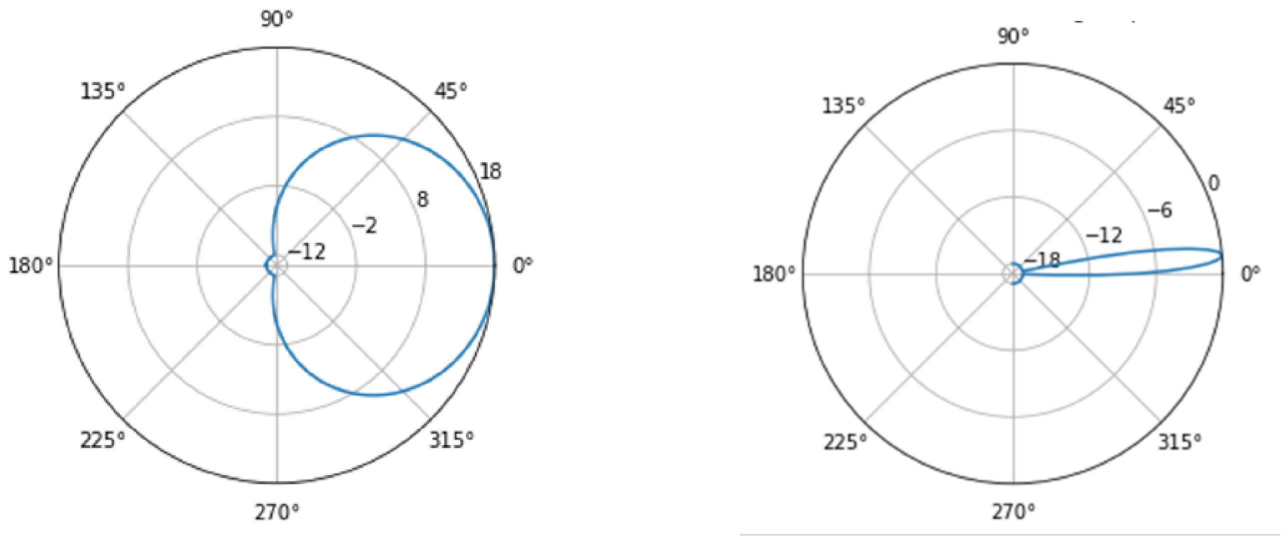

(i) Horizontal antenna gain [dB].

(ii) Vertical antenna gain [dB].

Figure 3.4: Horizontal and vertical antenna gains for a backfround cell.

3.3 Target modeling

We model the sensing targets as spherical objects to facilitate the simulation, since this allows us to (i) assume that the target radiates isotropically, therefore independent from the geometry of the system and (ii) simplify the expression of the Radar Cross Section (RCS), which is an indicator of how detectable an object is by the radar. Physically it represents the equivalent area of the sensing target that reflects signal power towards the sensing receiver and it is dependent on the shape, size, material of the object and the frequency of the illuminating signal [33]. Mathematically, the RCS is described as:

$$\gamma = \lim_{R\to\infty} 4\pi R^2 \frac{|E_s|^2}{|E_i|^2} \tag{3.3.1}$$

where R is the distance from the target to the sensing receiver, E_S is the scattered field strength at the sensing receiver and E_i is the incident field strength at the target.

However, according to [33], the RCS of a simple object, such as a sphere, can be approximated to an easier form. Furthermore, if the ratio $2\pi r/\lambda > 10$, where r is the radius of the sphere and λ is the wavelength of the signal, it means that the RCS of the object resides in the optical region, in other words it approaches a constant value which is independent of the frequency f. We can then approximate (3.3.1) by:

$$\gamma = \pi r^2 \tag{3.3.2}$$

Since our system operates at a frequency $f = 7.1875$ GHz, which means a wavelength of $\lambda = 4.17$ cm, for the RCS to reside in the optical region the spherical target needs to have a circumference $C = 41.7$ cm, corresponding with a radius of $r = 6.64$ cm. Assuming this value for r, the resulting RCS is $RCS = \pi 6.64^2 \approx 139\ cm^2 = 0.0139\ m^2$. Therefore, any value of RCS greater than or equal to 0.0139 m^2 assumed in this work ensures operation within the optical region. In this study, we consider RCS values within the range 1 m^2 $\leq$ RCS $\leq$ 100 m^2, which spans typical values from small objects to large airplanes.

3.4 Channel modeling

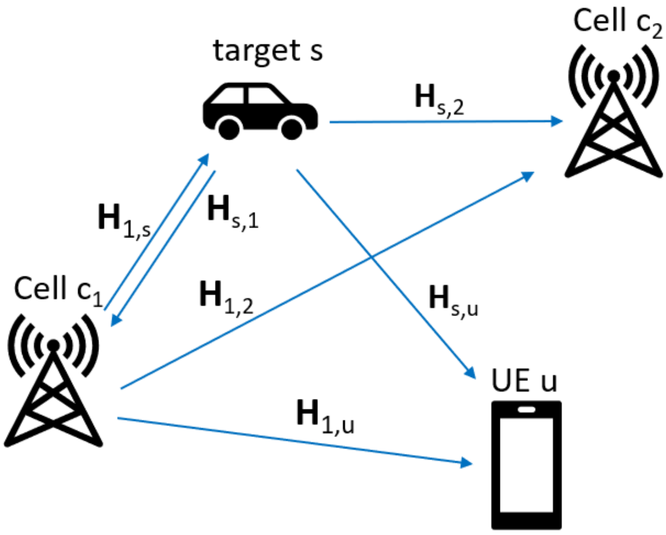

Figure 3.5: Radio propagation channel model.

The channel model adopted in this work is shown in Figure 3.5. Given a cell c which can act both as sensing transmitter and receiver equipped with n_c antennas, the UE equipped with n_{UE} antennas and sensing target s modelled as a single antenna object, a channel exists at TTI t and PRB f, represented by the channel response matrix $\mathbf{H}(t, f)$ between each of the following four links:

1. link between a cell c and a target s:

   $\mathbf{H}_{c,s}(t, f) \in \mathcal{C}^{n_c} \ \forall \ s \in \mathcal{O}, c \in \mathcal{C}, f \in \mathcal{F}$

2. link between a cell c_1 and another cell c_2:

   $\mathbf{H}_{c_1,c_2}(t, f) \in \mathcal{C}^{n_{c_1} \times n_{c_2}} \ \forall \ c_1, c_2 \in \mathcal{C}, f \in \mathcal{F}$

3. link between a cell c and a UE u:

   $\mathbf{H}_{c,u}(t, f) \in \mathcal{C}^{n_c \times n_u} \ \forall \ c \in \mathcal{C}, u \in \mathcal{U}, f \in \mathcal{F}$

4. link between a target s and a UE u:

   $\mathbf{H}_{s,u}(t, f) \in \mathcal{C}^{n_u} \ \forall \ s \in O, u \in \mathcal{U}, f \in \mathcal{F}$

where $\mathcal{O}$ denotes the set of target objects, $\mathcal{C}$ denotes the set of cells, $\mathcal{F}$ denotes the set of PRBs and $\mathcal{U}$ denotes the set of UEs. We assume that each channel link is symmetric, e.g. $\mathbf{H}_{1,s} = \mathbf{H}_{s,1}$.

In our model, we chose to do wideband precoding and combining which means that the precoding and combining are done over a wideband-equivalent channel. This wideband channel is represented as $\bar{\mathbf{H}}(t)$ and can be calculated by:

$$\bar{\mathbf{H}}(t) = \frac{\sum_{f \in \mathcal{F}} \mathbf{H}(t, f)}{|\mathcal{F}|} * \frac{\sum_{f \in \mathcal{F}} |\mathbf{H}(t, f)|}{|\sum_{f \in \mathcal{F}} \mathbf{H}(t, f)|} \tag{3.4.1}$$

where $\mathbf{H}(t, f)$ can be any of the four channel links described above.

In Equation 3.4.1, the average of the absolute channel gains over all PRBs is multiplied with the normalized sum of the channel over the number of PRBs.

Each channel comprises of an average channel gain $G^{av} \in \mathbb{R}$ and a time/frequency-varying multi-path fading channel $\mathbf{H}^{small-scale}(t,f) \in \mathcal{C}$. This is described for a general link between x and y entities/nodes by:

$$\mathbf{H}_{xy}(t,f) = \sqrt{G^{av}_{xy}} * \mathbf{H}^{small-scale}_{xy}(t,f) \tag{3.4.2}$$

Section 3.5 provides a detailed description of the average channel gain, while Section 3.6 focuses on the multi-path fading channel.

3.5 Average channel gain

We model the average channel gain for the four given links considering various factors such as Path Loss (PL), shadowing (S) and Antenna Gain (AG). A Minimum Coupling Loss (MCL) of 70 dB is assumed to avoid unrealistically small losses over short distances [34]. The general average channel gain for the four links described earlier can be written as follows:

$$G^{av}_{xy}(dB) = -max(PL_{x,y} + S_{x,y} - AG_{x,y}, MCL) \tag{3.5.1}$$

Each of these losses is described in detail below.

Path Loss

In this work we adopt the PL model defined in 3GPP's technical report TR38.901 [30] for the scenario Urban Macro (UMa) Non Line of Sight (NLoS) as:

$$PL_{UMa-NLOS} = max(PL_{UMa-LOS}, PL'_{UMa-NLOS}) \tag{3.5.2}$$

where $PL_{UMa-LOS}$ is the PL for the Line of Sight (LoS) scenario, which is defined at length in [30], and $PL'_{UMa-NLOS}$ is defined as:

$$\begin{aligned} PL'_{UMa-NLOS} = 13.54 + 39.08log_{10}(d_{3D}) + 20log_{10}(f_c) - 0.6(h_{UE} - 1.5)\ \ | \\ 1.5m \leq h_{UE} \leq 22.5m, h_{bs} = 25m \end{aligned} \tag{3.5.3}$$

where d_{3D} is the distance between the cell and the user in the 3-dimensional space, h_{UE} is the height of the UE, h_{bs} is the height of the BS and f_c is the center frequency of operation.

Shadowing

The shadow fading, or slow fading, is represented by a zero-mean Gaussian random variable Z with standard deviation σ and correlation ρ. σ is chosen to be 6 dB in outdoor users/targets scenario [30] and ρ is chosen to be 0.5 [35].

Figure 3.6 describes the shadowing relations between a cell c, UE 0 and target s. For each entity we first sample a shadowing value from the normal distribution Z_s, Z_c, Z_0 $N(0, \sigma^2)$. Then we determine the shadowing value for each link, for instance the link $Z_{c,0}$, as:

$$Z_{c,0} = Z_c\sqrt{\rho} + Z_0\sqrt{1-\rho} \tag{3.5.4}$$

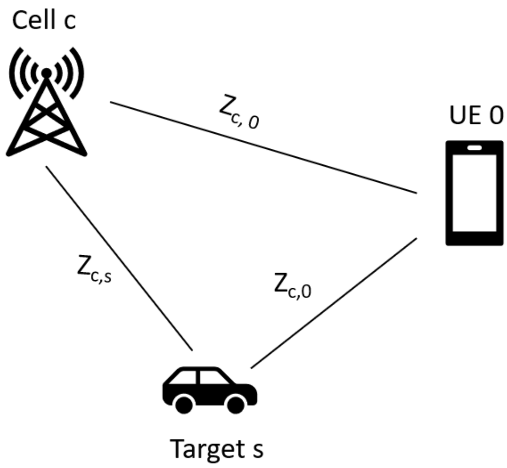

Figure 3.6: Visual representation of the shadowing model between cell c, UE 1 and target s.

3.6 Time-and-frequency-varying channel modeling

To implement the small-scale fading of the channels defined in Section 3.4 we use QuaDRiGa [36]. We model the local character of the user and target mobility by creating a circular track of radius 0.5m where the user/target moves at a speed of 0.8m/s. The channel model for all links is based on the UMa NLoS scenario, as shown in Equation 3.5.2.

Ideally, we would model the channels of each entity individually. However, this would require implementing a complex slot-level structure, as generating a complete set of traces for each entity would cause the computational complexity of the simulation to increase dramatically. To mitigate this, we instead create a randomized set of generic traces at arbitrary entity positions. For each specific link, we then randomly select one of these generic traces and adapt it to the particular cell-entity orientations involved. To achieve this adaptation, we first remove the phases from the channel traces generated for the arbitrary positions, making them phaseless, using the following equation:

$$\mathbf{H}^{small-scale}_{trace,phaseless}[i,j] = e^{j2\pi d_{ij}/\lambda} * \mathbf{H}^{small-scale}_{trace,original}[i,j] \quad \forall i = \{0,1,..,n_{tx}-1\}, j \in \{0,...,n_{rx}-1\} \tag{3.6.1}$$

where d_{ij} is the distance between i_{th} antenna element of the BS and the j_{th} antenna element of the entity. To avoid confusion, we remind the reader that, although the sensing target lacks any physical antenna, we model it as a single-antenna object for the purposes of the simulation.

Next, for each link, we randomly select one of these processed generic traces, along with a random starting point. Finally, a distance-based phase (distance for the actual entity location) is added back to the trace using:

$$\mathbf{H}^{small-scale}_{trace,phases}[m,n](t,f) = e^{-j2\pi d_{mn}/\lambda} * \mathbf{H}^{small-scale}_{trace,phaseless}[m,n] \quad \forall m = \{0,1,..,n_{tx}-1\}, n \in \{0,...,n_{rx}-1\} \tag{3.6.2}$$

where d_{mn} is the distance between m_{th} antenna element of the BS and the n_{th} antenna element of the entity.

Chapter 4

SINR, throughput and probability of detection

The SINR is a key performance metric in wireless communication systems that quantifies the quality of a received signal in the presence of both interference and background noise. Specifically, SINR is the ratio of the power of a desired signal to the combined power of interference from other transmitters and the ambient noise present in the system.

In this section we derive the SINR calculations for both the communication and the sensing tasks and we show how to compute the user's throughput and the target's probability of detection given the experienced SINR.

4.1 Communication SINR and throughput

We calculate the $SINR_u(t, f)$ for the user u, associated to cell c^u , at TTI t and PRB f as:

$$SINR_u(t, f) = \frac{1}{(\sum_{rx=0..(n_{rx}-1)} |\mathbf{v}_u[rx](t, f)|^2)N_0 + I_{u,intra}(t, f) + I_{u,inter}(t, f)} \tag{4.1.1}$$

where, $\mathbf{v}_u(t, f)$ is the combiner of user u derived as:

$$\mathbf{v}_u(t, f) = ((\sqrt{P_u}\mathbf{w}_u(t))\mathbf{H}_u(t))^+ \tag{4.1.2}$$

which differs from the combiner derived in Equation 5.4.1 because the transmit power P_u towards user u is incorporated in the precoder $\mathbf{w}_u(t)$. N_0 denotes the effective noise power and $I_{u,intra}(t, f)$, $I_{u,inter}(t, f)$ denote the intra-cell and inter-cell interference, respectively. These are described in detail in the next paragraphs.

Noise modeling

The effective noise power N_0 is calculated as:

$$N_0 = KTB \times 10^{NF/10} \tag{4.1.3}$$

where K is the Boltzmann constant, i.e., 1.38×10^{-23} Joules-per-Kelvin, T is the thermal noise temperature taken as 290 Kelvin, NF is the receiver noise figure of 8 dB for the UEs and 2 dB for the BSs, and B is the bandwidth over which we calculate the SINRs, which in our case is the bandwidth of a PRB, which is 360 kHz.

Interference modeling

1. Intra-cell interference: this refers to the interference experienced by a user u generated by its own cell c^u at TTI t and PRB f to serve another entity e:

$$I_{u,intra}(t,f) = \sum_{e \in E^S_{c^u}(t) \setminus \{u\}} P^e_{T,PRB}(t) |\mathbf{v}_u(t,f)\mathbf{H}_{c^u,u}(t,f)\mathbf{w}_{c^u,e}(t)|^2 \tag{4.1.4}$$

where, $E^S_{c^u}(t)$ is the set of scheduled entities at TTI t in cell c^u, $P^e_{T,PRB}$ is the power transmitted to the entity e per PRB, which is equal to the total power allocated to the entity e equally divided among PRBs.

2. Inter-cell interference: this refers to the interference experienced by a user u generated by neighbouring cells using the same resource block of TTI t and PRB f to serve another entity e. In our work, we make a distinction between the evaluation cells (the seven inner cells) and the background cells (the outer twelve cells):

$$I_{u,inter}(t,f) = I_{u,inter,evaluation}(t,f) + I_{u,inter,background}(t,f) \tag{4.1.5}$$

where

$$I_{u,inter,evaluation}(t,f) = \sum_{c \in \{0..6\} \setminus \{c^u\}} \sum_{e \in E^S_c(t)} P^e_{T,PRB}(t) |\mathbf{v}_u(t)\mathbf{H}_{c,u}(t,f)\mathbf{w}_{c,e}(t)|^2 \tag{4.1.6}$$

and

$$I_{u,inter,background}(t,f) = \sum_{c \in \{7..18\}} \delta_p P_{T,PRB}(t) |\mathbf{v}_u(t)\mathbf{H}_{c,u}(t,f)\mathbf{n}_{uniform}|^2 \tag{4.1.7}$$

where δ_p is a tunable parameter to control the amount of interference generated by the outer cells and $\mathbf{n}_{uniform}$ is a uniformly normalised vector of dimension $[n_{tx}, 1]$, which is essential to reshape $\mathbf{H}_{c,u}(t,f)$ from its original dimension $[n_{rx}, n_{tx}]$ to $[n_{rx}, 1]$ since the background cells are modeled as a single antenna sub-array as explained in Section 3.2.

Previously, we computed SINR values on a per PRB basis. However, our focus is on evaluating SINR across the entire carrier bandwidth because transport blocks are transmitted over the full carrier and we need to evaluate the SINR at the transport block level so we can map it to a throughput value. We can achieve this by using the Mutual Information Effective SINR Mapping (MIESM) method [37]. This method allows us to determine the effective SINR $SINR^u_{eff}$ for a specific user u across all PRBs. The process involves two main steps: converting $SINR_u(t,f)$ values into mutual information $MI_u(t,f)$ and then averaging $MI_u(t,f)$ to obtain $MI^u_{eff}(t)$. Subsequently, $MI^u_{eff}(t)$ is mapped back to determine $SINR^u_{eff}(t)$ using Modulation and Coding Scheme (MCS)-dependent curves, shown in Figure 4.1, specifically choosing the curve corresponding to 256 Quadrature Amplitude Modulation (QAM) modulation for this thesis. Since we use a Shannon-based data rate calculation, and not adopt a MCS (modulation and coding scheme) dependent rate control algorithm, we assume the MCS to be 256 QAM, which provides the best data rate and spectral efficiency.

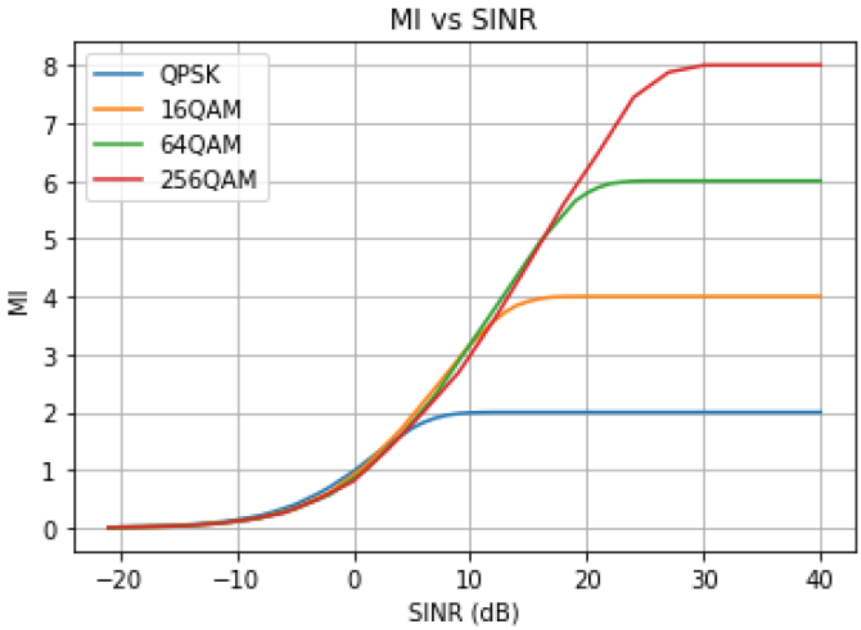

Figure 4.1: MI vs SINR curves for different modulation order [37].

4.1.1 Throughput calculation

Finally, we can compute the data rate experienced by user u at TTI t using the truncated Shannon rate formula, as shown below:

$$R_u = \min\{R_{max}, CF * Blog_2(1 + SINR_u^{eff})\} \tag{4.1.8}$$

Here, $R_{\max}$ represents the maximum achievable rate of 114.752 Mbps, as shown in Section 5.1.3.2 of [38]. The Correction Factor (CF) is modeled to consider resources consumed by control signaling and inaccuracies in channel estimations. A value of 0.75 for CF is chosen based on typical ranges of such correction factors documented in [39].

4.2 Sensing SINR and probability of detection

First we show how to compute the SINR in the sense of a simple scenario, and then we generalise it in the sense of a more complex one.

4.2.1 Simple scenario: single-transmitter single-receiver sensing topology

The considered scenario is illustrated in Figure 4.2. It consists of one communication task and one sensing task. The communication task involves downlink communication between cell a and UE 1. The sensing task focuses on detecting target s, where cell a acts as the sensing transmitter and UE 0 as the sensing receiver. Here, $\mathbf{H}$ represents the channel response matrix as derived in Equation 3.4.2, $\mathbf{w}$ is the precoding vector derived in Equation 5.3.3, and P denotes the transmit power for each task. In this section, we derive the expression for the received SINR of the reflected sensing signal at UE 0.

The equation for $\mathbf{s}(t, f)$, denoting the received power of sensing signals at each antenna element in the receiving node, is derived starting from the classical radar equation, which calculates the power received by a single-antenna radar receiver at time t and frequency f [40]:

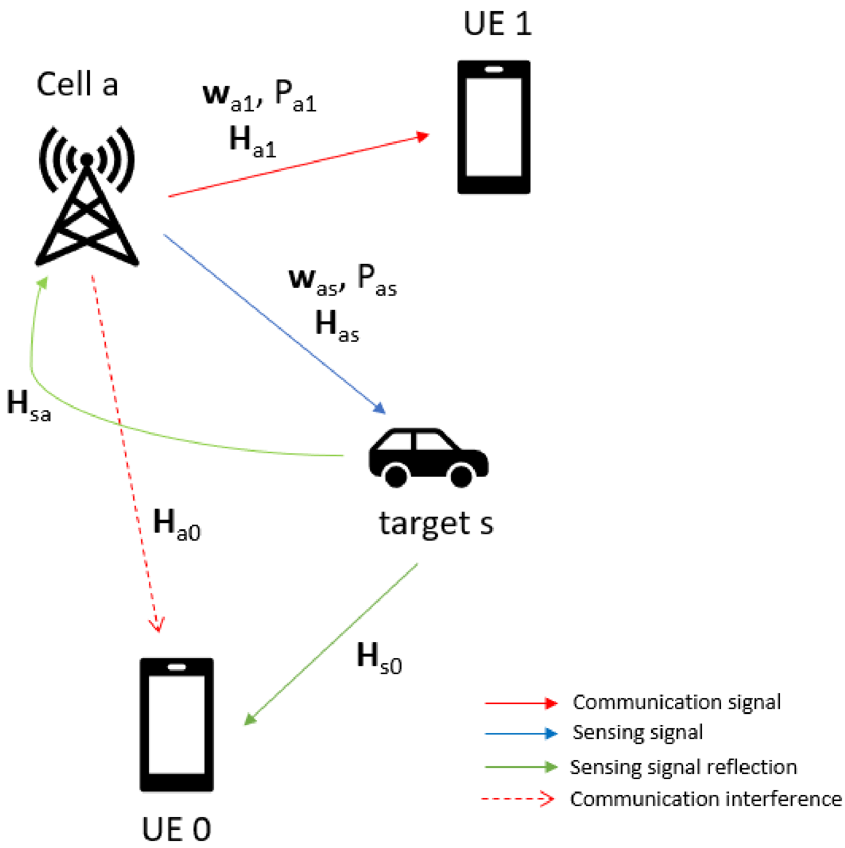

Figure 4.2: Simple scenario for target detection with a single-transmitter single-receiver sensing topology.

$$S(t,f) = \frac{PG_tG_r\lambda^2\gamma}{(4\pi)^3R_T^2R_R^2L} \tag{4.2.1}$$

where P is the transmitted power, G_t and G_r are the transmitting and receiving antenna gains, λ is the wavelength, γ is the RCS of the target, R_T and R_R are the distances between the transmitter, target, and receiver, respectively, and L represents system losses such as hardware imperfections [40].

While Equation 4.2.1 assumes free-space path loss, our model considers 3GPP UMa NLoS path-loss, requiring an adaptation of the equation. Additionally, we rewrite the gains and losses in terms of the precoding and channel models adopted in this work. First, we expand the path-loss components of Equation 4.2.1, leading to Equation 4.2.2:

$$S(t,f) = \frac{PG_tG_r\gamma}{\frac{(4\pi R_T)^2}{\lambda^2}\frac{(4\pi R_R)^2}{\lambda^2}\frac{\lambda^2}{4\pi}L} \tag{4.2.2}$$

Here, $\frac{(4\pi R_T)^2}{\lambda^2}$ and $\frac{(4\pi R_R)^2}{\lambda^2}$ represent the path-loss for the links between the transmitter, target and receiver, respectively, and $\frac{\lambda^2}{4\pi}$ is the effective aperture of an isotropic receiving antenna, as it is assumed in the free-space path-loss derivation [41]. However, the gains and losses in this equation are already accounted for in our path-loss model, allowing us to simplify and express it as:

$$\mathbf{s}(t,f) = P_{a,s}|\mathbf{H}_{a,s}\mathbf{w}_{a,s}|^2\frac{\gamma}{\lambda^2/4\pi}(abs(\mathbf{H}_{s,0}))^2 \tag{4.2.3}$$

In Equation 4.2.3, the classical radar equation is adapted to align with the wireless channel and precoding models used in this work. The received power depends on the channel response matrices $\mathbf{H}_{a,s}$ and $\mathbf{H}_{s,0}$, which account for both path loss and antenna gains, as well as the precoding vector $\mathbf{w}_{a,s}$, yielding a beamforming gain. The antenna gains and system losses, initially represented in the radar equation, are now appropriately captured in Equation 4.2.3.

Now we want to combine the received signal powers $\mathbf{s}(t, f)$ at each of the receive antennas to obtain the total received power $S(t, f)$ at UE 0, TTI t and PRB f. According to the coherent combining formula commonly used in the sensing literature [42], we can implicitly combine the received signal powers by summing their amplitude, as shown in Equation 4.2.4:

$$S(t, f) = \left(\sum_{rx=0..(n_{rx}-1)} \sqrt{\mathbf{s}[rx](t, f)} \right)^2 \tag{4.2.4}$$

where $\mathbf{s}[rx](t, f)$ is the received signal power at the receive antenna rx of UE 0 at TTI t and PRB f.

Next, to compute the SINR we need to compute the interference experienced by the sensing receiver. From Figure 4.2, we can identify two sources of interference. We define $I_{communication}$ as the interference generated by the communication task and $I_{sensing}$ as the interference generated by the sensing task. The interference generated by the communication task at the receiver is computed as:

$$I_{communication}(t, f) = \sum_{rx=0..(n_{rx}-1)} \left(P_{a,1} \, |\mathbf{H}_{a,0}[rx]\mathbf{w}_{a,1}|^2 \right) \tag{4.2.5}$$

while interference generated by the sensing task is computed as:

$$I_{sensing}(t, f) = \sum_{rx=0..(n_{rx}-1)} P_{a,s} |\mathbf{H}_{a,0}[rx]\mathbf{w}_{a,s}|^2 \tag{4.2.6}$$

Therefore, the total interference experienced by the receiver antenna elements would be $I(t, f) = I_{communication}(t, f) + I_{sensing}(t, f)$. However, in radar applications, a two-dimensional Rang-Doppler diagram is utilized to identify objects by analyzing the frequency shift in the returned radar signal, which results from the motion between the radar system and the object. This frequency shift facilitates the differentiation between stationary and moving targets. To mitigate interference from static sources and low-velocity objects, specific signal processing filters are employed. These filters efficiently suppress signals from objects that do not match the velocity and direction of the target of interest, thereby focusing on relevant moving targets [42]. It is important to note that the energy from filtered out signals cannot be eliminated completely, therefore, we introduce two tunable parameters in our model, β_c and β_s, which quantify the impact of communication and sensing interference on the SINR. Since in our model the sensing targets are moving at walking speed, the value of both parameters needs to be close to one. In our simulation we assume $\beta_c = 1$ and $\beta_s = 1$, thus considering a worst-case scenario. We can now derive the formula of the interference experienced by a sensing receiver at TTI t and PRB f as:

$$I(t, f) = \beta_c I_{communication}(t, f) + \beta_s I_{sensing}(t, f) \tag{4.2.7}$$

Finally, to compute the Pd, we are interested in computing the SINR over the wide-band channel. Due to the possible frequency-selective fading and different multi-path environment at different PRBs, we have to combine the SINR values at TTI t over all PRBs incoherently, as derived in Equation 4.2.8 [42]:

$$SINR(t) = \frac{\sum_{f=0..(n_{prb}-1)} S(t, f)}{\sum_{f=0..(n_{prb}-1)} (N_0 + I(t, f))} \tag{4.2.8}$$

In this simple scenario we derived the SINR calculations for a single-transmitter single-receiver sensing system performing a sensing task at a given TTI t. In the next subsection we present the derivation of SINR calculations when a multi-transmitter multi-receiver sensing system is used to perform a sensing task.

4.2.2 Complex scenario: multi-transmitter multi-receiver sensing topology

In this subsection, we extend the derivation of the SINR to a more complex scenario involving multiple cells and UEs within the considered network. Here, we explore the potential for sensing tasks to be executed through cooperative efforts, involving clusters of transmitting and receiving cells and UEs, denoted as sensing topologies. These topologies operate collaboratively, as depicted in Figure 4.3. In this figure, the sensing topology responsible for detecting the target s comprises two cells: cell a, which serves as both the sensing transmitter and receiver, and cell c, which serves as an additional sensing transmitter. Additionally, two UEs, UE 0 and UE 1, serve as sensing receivers. Simultaneously, cell b, cell c, UE 0, and UE 1 participate in communication tasks, introducing communication interference into the detection of target s. Moreover, cell a and cell b, which are involved in detecting target r, contribute to sensing interference.

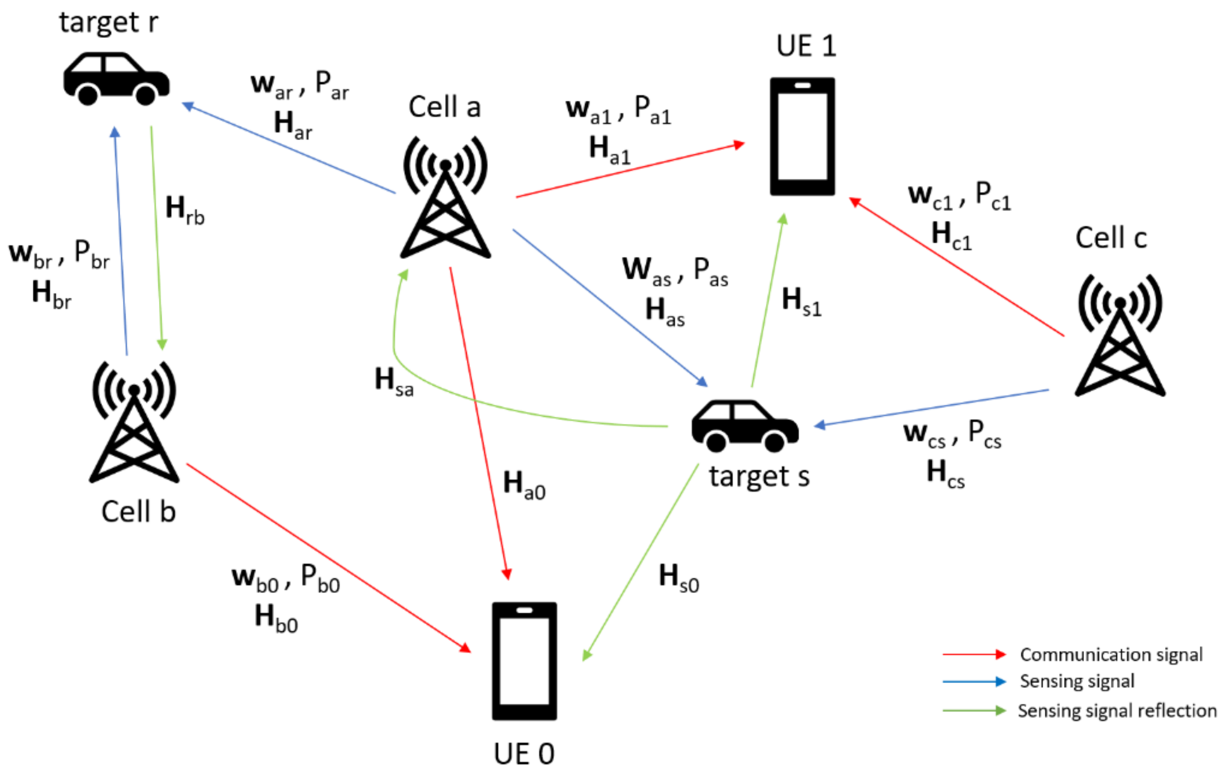

Figure 4.3: Complex scenario for target detection with a multi-transmitter multi-receiver sensing topology.

Since the sensing task is now performed by multiple sensing transmitters and receivers, we can analyze each link between a transmitter node x_{tx} and a receiver node x_{rx} individually, as derived in Section 4.2.1. For each link (x_{tx}, x_{rx}), we can apply Equation 4.2.3 in combination with Equation 4.2.4 to compute the received power $S_{x_{tx},x_{rx}}(t, f)$ at x_{rx} from the sensing signal transmitted by x_{tx}. In scenarios with multiple transmitters, each receiver will accumulate signal power from each one of the transmitters. To calculate the total received power at the topology level, which contributes to the overall SINR, we need to combine these individual power contributions.

As discussed in Section 4.2.1, there are two methods for combining received signal powers in the sensing literature: *coherent* combining, introduced in Equation 4.2.4, and *incoherent* combining, introduced in Equation 4.2.8. In this work, we assume that the cells in the network are interconnected via a backhaul link with sufficient capacity to ensure perfect synchronization between them. This enables *coherent* combining of the received signal powers across different cell-based receivers, as the synchronization ensures that the signals are in phase, allowing their amplitudes to be directly summed. This process is described in Equation 4.2.9:

$$S_{coherent}(t,f) = \left(\sum_{x_{tx} \in \mathcal{TX}} \sum_{c \in \mathcal{RX}} \sqrt{S_{x_{tx},c}(t,f)} \right)^2 \tag{4.2.9}$$

where $\mathcal{TX}$ and $\mathcal{RX}$ are the sets of transmitters and receivers in the sensing topology, respectively. The variable c denotes a cell-based receiver selected in the sensing topology, and $S_{x_{tx},c}(t,f)$ represents the received sensing power over the link (x_{tx}, c).

Conversely, the UE serving as sensing receivers cannot be considered synchronized with the other receiving nodes. As a result, their power contributions must be combined *incoherently* with $S_{coherent}(t,f)$ computed in Equation 4.2.9. This results in $S(t,f)$, the total combined received signal power at TTI t and PRB f across the receivers in the sensing topology, as expressed in Equation 4.2.10:

$$S(t,f) = S_{coherent}(t,f) + \sum_{x_{tx} \in \mathcal{TX}} \sum_{u \in \mathcal{RX}} S_{x_{tx},u}(t,f) \tag{4.2.10}$$

where u denotes a UE-based receiver within the sensing topology, and $S_{x_{tx},u}(t,f)$ represents the received sensing power over the link (x_{tx}, u).

Now, we need to compute the total combined experienced interference across all the receiving nodes in the sensing topology. The communication and sensing interference experienced by a receiving node x_{rx} in the sensing topology, are computed extending Equations 4.2.5 and 4.2.6 to combine the interference contributions generated by multiple transmitters. Finally, the total combined communication interference $I_{communication}(t,f)$ of the sensing topology at TTI t and PRB f is computed as the sum of all interferences experienced at each receiving node x_{rx} as:

$$I_{communication}(t,f) = \sum_{x_{rx} \in \mathcal{RX}} \sum_{c \in \mathcal{C}} \sum_{u \in \mathcal{U}_c^S} \sum_{rx=0..(n_{rx}-1)} P_{c,u} |\mathbf{H}_{c,x_{rx}}[rx] \mathbf{w}_{c,u}|^2) \tag{4.2.11}$$

where $\mathcal{C}$ is the set of cells in the network, $\mathcal{U}_c^S$ is the set of users scheduled at cell c and TTI t, and $\mathcal{RX}$ is the set of receiving nodes in the sensing topology. The sensing interference $I_{sensing}(t,f)$ is derived very similarly to the communication interference $I_{communication}(t,f)$ as:

$$I_{sensing}(t,f) = \sum_{x_{rx} \in \mathcal{RX}} \sum_{c \in \mathcal{C}} \sum_{s \in \mathcal{S}_c^S \setminus \{s_0\}} \sum_{rx=0..(n_{rx}-1)} P_{c,s} |\mathbf{H}_{c,x_{rx}}[rx] \mathbf{w}_{c,s}|^2) \tag{4.2.12}$$

where $\mathcal{C}$ is the set of cells in the network, $\mathcal{S}_c^S$ is the set of sensing tasks scheduled at cell c and TTI t, and $\mathcal{RX}$ is the set of receiving nodes in the sensing topology and s_0 is the considered sensing task.

Now that we have defined $I_{communication}(t,f)$ and $I_{sensing}(t,f)$, the total interference $I(t,f)$ experienced by a sensing topology at TTI t and PRB f is computed according to Equation 4.2.7.

To compute the noise at a receiving node $N_{x_{rx}}(t,f)$ at TTI t and PRB f, we follow the expression derived in Equation 4.1.3 and, to compute the total noise power $N(t,f)$ experienced by a sensing topology, we sum the noise contributions of each individual receiver node in the sensing topology as:

$$N_{tot}(t,f) = \sum_{x_{rx} \in \mathcal{RX}} N_{x_{rx}}(t,f) \tag{4.2.13}$$

Analogously to Section 4.2.1, to compute the total combined SINR $SINR(t)$ for a sensing topology over the wideband channel, all the total received powers $S(t,f)$ are incoherently combined across all PRBs as [42]:

$$SINR(t) = \frac{\sum_{f \in 0..(n_{prb}-1)} S(t,f)}{\sum_{f \in 0..(n_{prb}-1)} (N(t,f) + I(t,f))} \tag{4.2.14}$$

4.2.3 Probability of detection calculation

Once the received SINR is computed, the Pd can be determined using the curves in Figure 4.4, based on the chosen Probability of False Alarm (Pfa) [43]. The Pfa represents the probability that the system will incorrectly signal the presence of a target when none exists. In radar systems, reducing the Pfa necessitates a higher measured SINR to achieve the same level of detection confidence compared to operating with a higher Pfa. As noted in [43], "A typical radar system operates with a detection probability of 0.9 and a probability of false alarm of 10^{-6}."

According to [43], the curves in Figure 4.4 map a range of SINR values to a range of Pd for a given Pfa based on a single SINR measurement. However, our network operates over 51 PRBs, resulting in 51 separate measurements. While the received power values are combined incoherently, detection theory provides methods to enhance the resulting Pd, as combining multiple measurements increases confidence, even if the SINR itself does not improve. Unfortunately, due to the time constraints of this thesis research, we were unable to implement these methods in our model. Therefore, we propose this as future work. As a result, our current results represent a worst-case and hence conservative scenario, as Pd values obtained with these techniques would likely be more optimistic.

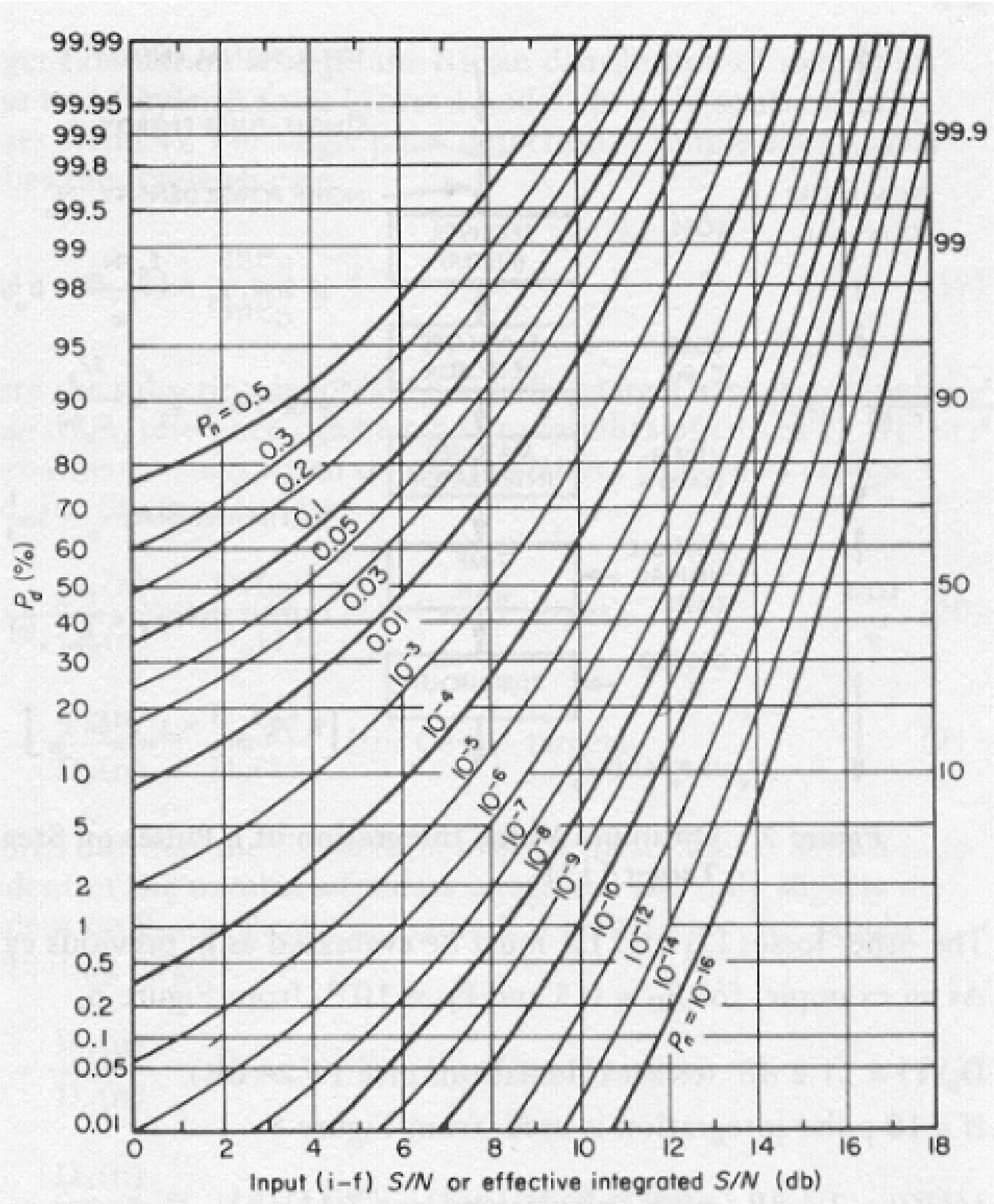

Figure 4.4: Pd as a function of SNR with false alarm probability as a parameter assuming a single pulse sinusoidal signal in Gaussian noise [43].

Chapter 5

Resource management solutions

In this chapter we present the Radio Resource Management (RRM) solutions adopted in this work for both sensing tasks and communication flows.

5.1 Sensing topology management

The sensing topology management comprises of two parts: (i) sensing topology selection and (ii) dynamic node contribution management.

5.1.1 Sensing topology selection

The sensing topology selection algorithm is executed at the start of each simulation snapshot for every sensing task, aiming to identify the set of BSs and/or UEs that will collaboratively perform the given sensing task and assign specific roles to each of the selected nodes, designating them as transmitters, receivers, or both.

The sensing topology selection process is divided into two stages: (i) the identification of suitable nodes for a particular sensing task, and (ii) the actual selection of nodes to be included in the topology, along with the assignment of their respective roles.

Selection of nodes

We denote the set of candidate nodes as $\mathcal{X} \subset \mathcal{U}_{sensing} \cup \mathcal{C}$, where $\mathcal{U}_{sensing}$ denotes the set of UEs in the network available to participate in a sensing task and $\mathcal{C}$ denotes the set of all cells. The gain $G^{av}_{x,s}$ for each link between the target s and every available node x in the network is computed according to Equation 3.5.1. The average gain is used here instead of the TTI-specific time/frequency-varying gain derived in Equation 3.4.2 because performing the topology selection algorithm at the TTI level would introduce unmanageable overhead, as it would require informing all nodes of any changes in topology.

Once the average gains have been computed for each link, the nodes are ranked according to their respective gains. The node experiencing the highest gain is selected to be part of the sensing topology. In addition to this node, all other nodes that fulfill the requirement in Equation 5.1.1 are selected:

$$G^{av}_{x_i,s} \geq G^{av}_{x_0,s} - G_{th} \;\; \forall \;\; x_i \in \mathcal{X} \setminus \{x_0\} \tag{5.1.1}$$

where $G^{av}_{x_0,s}$ is the highest average gain and G_{th} is a configurable parameter in the simulation. The only constraint imposed on the sensing topology is that it must include at least one transmitting and one receiving node. Since UEs can only serve as sensing receivers, it is necessary to ensure that at least one cell is selected for each topology. Consequently, if no average gain between a cell c and the target s satisfies the aforementioned condition, the cell with the highest gain among the set of cells $\mathcal{C}$ is selected to be part of the sensing topology.

Assignment of roles

The role assignment algorithm conducts an exhaustive search through all possible topologies, considering all combinations of transmitters, receivers, or both, based on the selected nodes. Ideally, this algorithm would select the topology that achieves the highest combined SINR for the received sensing signals, leading to a higher Pd. However, this is not feasible because two factors are unknown: (i) the TTI-specific time-frequency varying channels, and (ii) the precise interference and resource multiplexing effects introduced by communication flows or other sensing tasks. Therefore, we approximate the SINR using SNR calculations to select the best topology.

For each candidate topology, we estimate the resulting SNR by following the steps outlined below:

1. **Step 1:** Estimate the received signal powers from all the transmitting nodes x_{tx} to each of the receiving nodes x_{rx} selected in the topology:

$$S_{x_{rx}} = \left(\sum_{x_{tx} \in \mathcal{X}_{tx}} \sum_{rx \in RX} \sqrt{P_{max} \mathbf{H}_{x_{tx},s} \mathbf{w}_{x_{tx},s} \frac{\gamma}{\lambda^2/4\pi} \mathbf{H}_{s,x_{rx}}} \right)^2 \tag{5.1.2}$$

   where P_{max} is the maximum available power at the transmitter, $\mathbf{w}_{x_{tx},s}$ is the Maximum Ratio Transmission (MRT) precoder derived according to Equation 5.3.1, and the received powers are coherently combined according to Equation 4.2.4.

2. **Step 2:** Estimate the overall SNR of the sensing topology, $S_{topology}$, by first summing the received powers $S_{x_{rx}}$ at each receiver node as follows:

$$S_{topology} = \left(\sum_{c \in \mathcal{X}_{rx}} \sqrt{S_{x_{rx}}} \right)^2 + \sum_{u \in \mathcal{X}_{rx}} S_{x_{rx}} \tag{5.1.3}$$

   where c denotes a receiving cell and u denotes a receiving UE selected in the sensing topology.

3. **Step 3:** Compute the estimated SNR as:

$$SNR_{topology} = \frac{S_{topology}}{\sum_{x_{rx} \in \mathcal{X}} N_0} \tag{5.1.4}$$

Finally, given the set of selected nodes, the algorithm will choose the sensing topology that includes these nodes, along with their respective role assignments, based on the configuration that experiences the highest SNR estimate.

5.1.2 Dynamic node contribution management

Once the topology achieving the highest estimated SNR is selected for a sensing task s, it will be used to compute the total SINR throughout the whole simulation snapshot. However, since the totopology was selected according to the highest estimated SNR and not SINR, it will lead to suboptimal results when nodes, especially far away from the target s, receive higher interfereing power than the sensing signal reflection power, thus worsening the combined SINR of the topology. Therefore, every node serving as a sensing receiver in the topology has the choice to not contribute to the detection task at the assumed TTI t if:

$$S_{n_{rx}}(t, f) < \beta_c I_{communication,n_{rx}} + \beta_s I_{communication,n_{rx}} + N_0 \tag{5.1.5}$$

Figure 5.1 shows a comparison in Pd performance where in (i) the dynamic node contribution management is disabled and in (ii) is enabled, in a scenario with one target, where the number of UEs available for sensing is varying and the analysis is performed over multiple sizes of topology. It is clearly visible that without the dynamic node contribution management enabled, the I+N becomes bigger than the S with growing topologies, while when it is enabled increasing the topology size has a positive impact.

Throughout the remainder of this thesis, we refer to the topology size selected by the sensing topology selection algorithm as the *selected topology*, while the modified topology at the TTI level, managed by the dynamic node contribution management algorithm, is referred to as the *effective topology*.

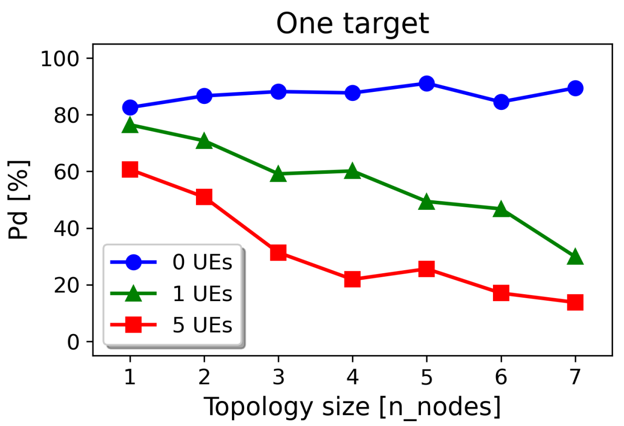

(i) PD comparison for 0, 1 and 5 UEs deployed for each evaluation cell one sensing task available.

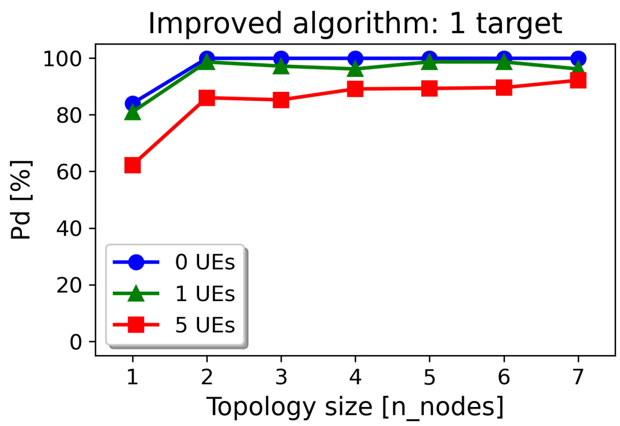

(ii) PD comparison for 0, 1 and 5 UEs deployed for each evaluation cell 1 sensing tasks available improved algorithm.

Figure 5.1: Performance of PD under varying topologies and UE configurations.

5.2 Cell-user association

Cell-user association is an RRM task whose goal it is to determine which cell a specific UE should be connected to. In this work we adopt the term user for the UE and we use these terms interchangeably.

In a 5G cellular network, all cells broadcast beams, namely Synchronization Signal Blocks (SSB)s, in a periodic manner. A given user u listens to these SSBs from all the cells and attempts a handshake with the cell from which it receives the strongest SSB. If it does not receive a sufficiently strong SSB from any cell then the user is considered out of coverage. Thus, a given user u, is associated to a given cell c^u with:

$$c^u = \arg\max_{c \in \mathcal{C}} (P_{c^u}^{SSB} \cdot G_{c,\epsilon,u}) \tag{5.2.1}$$

and,

$$P_{c^u}^{SSB} \cdot G_{c,\epsilon,u} \geq S_{th}^{SSB} \tag{5.2.2}$$

where $\mathcal{C}$ is a set of all cells, $P_{c^u}^{SSB}$ is the transmitted power of SSB ϵ in cell c, $G_{c,\epsilon,u}$ is the total propagation gain on that SSB to user u, and S_{th}^{SSB} is the threshold signal power needed for a user to connect to a cell. In this work we adopt $S_{th}^{SSB} = -110\ dBm$ [44].

5.3 Beamforming

Beamforming is an RRM task in which a wireless signal is aimed at a specific receiving device. This is achieved by applying a precoding vector to the signals fed to multiple transmit antennas. The precoding vector adjusts the amplitude and phase of each signal to optimize the overall signal strength and radio link quality (SINR) at the receiver. In this study, we utilize MRT precoding and Zero Forcing (ZF) precoding, which are defined below. We also assume that perfect Channel State Information (CSI) is known.

5.3.1 Maximum ratio transmission

MRT is a precoding technique that aims to maximize the gain of the radio link between a cell c and a user u. For a given user-antenna pair (u, rx), the precoder $\mathbf{w}_u$ is given by:

$$\mathbf{w}_{u,rx} = \frac{\mathbf{h}_{u,rx}^*}{\|\mathbf{h}_{u,rx}\|_2} \tag{5.3.1}$$

where, $\mathbf{h}_{u,rx}$ represents the wideband radio link channel response for a user-antenna pair (u, rx) from its associated cell c at time t.

MRT is particularly effective in Single-User Multiple-Input Multiple-Output (SU-MIMO) since it aims to optimise the user-specific beamforming gain, and consequently the received signal strength, without any regard for possible interference to other users.

5.3.2 Zero forcing

ZF is a precoding technique applied in Multi-User Multiple-Input Multiple-Output (MU-MIMO) designed to eliminate interference at the receiving users by ensuring that the transmitted signal is orthogonal to potential intra-cell interfering signals. The precoding matrix in ZF is calculated to nullify the intra-cell interference caused by transmitting antennas at the receiving end, while still achieving the highest attainable beamforming gains. The ZF precoder at cell c for all its scheduled users, denoted as $\mathbf{W}_c$ is calculated as [45]:

$$\mathbf{W}_c = (\mathbf{H}_c^T)^+ \tag{5.3.2}$$

where $\mathbf{H}_c^T$ denotes the wideband channel matrix comprising of channel vectors from the cell c to all the scheduled user-antenna pairs and $(\mathbf{H_c^T})^+$ is the Moore-Penrose pseudo-inverse of $\mathbf{H}_c^T$. Each column vector $\mathbf{h}_{u,rx}$ of $\mathbf{W}_c$, which represents the precoding vector for the user-antenna pair (u, rx) is then normalized by its L-2 norm to ensure that the transmit power P_{tx}, which is the summed transmit power over the users, does not exceed the maximum available transmit power P_{max} available at cell c as:

$$\hat{\mathbf{h}}_{u,rx} = \frac{\mathbf{h}_{u,rx}}{\|\mathbf{h}_{u,rx}\|_2} \tag{5.3.3}$$

where $\hat{\mathbf{h}}_{u,rx}$ is the normalized precoding vector user u.

5.4 Combiner

A combiner is a critical component in the receiver system of a multi-antenna communication setup. Its main function is to merge the signals received from different antennas, thereby enhancing their combined strength and exploiting the diversity offered by multiple antennas to improve the overall quality of the received signal. Maximum Ratio Combining (MRC) is the most common combiner technique, which maximizes the SINR by adjusting the weighting and the cophasing of the received signals based on their channel gains. It assigns greater weight to signals with higher channel gains and lesser weight to those with lower channel gains. This technique is particularly effective in mitigating fading and enhancing signal quality. In a SU-MIMO system, the MRC combiner, $\mathbf{v}_u(t)$ for user u at time t, is calculated as:

$$\mathbf{v_u}(\mathbf{t}) = (\mathbf{w}_u(t)\mathbf{H}_u(t))^+ \tag{5.4.1}$$

where, $\mathbf{w}_u(t)$ represents the precoder for user u and $\mathbf{H}_u(t)$ represents the wideband channel between the cell to the user u at time t.

5.5 Scheduling

In this section, we present the resource scheduling algorithm implemented for both sensing tasks and communication flows. We adopt slightly different definitions of scheduling for these tasks. Specifically, the communication scheduling algorithm is executed for each cell to schedule users at each TTI, while the sensing scheduling algorithm is executed only once at the beginning of the simulation. The primary role of the sensing scheduling algorithm is to time-schedule sensing tasks, as described below. However, instead of scheduling sensing tasks for a single cell, it schedules them for the entire sensing topology selected for the task. As a result, sensing scheduling is performed at the topology level, as opposed to the cell level.

5.5.1 Sensing tasks scheduling

Each sensing task must be performed with a specific periodicity, determined by the sensing period $T_{sensing} = n\ TTIs$.

The scheduling of sensing tasks is performed at the start of each simulation snapshot. The goal of this algorithm is to distribute the sensing tasks as evenly as possible across TTIs within the assumed sensing period. This schedule is then consistently repeated for all subsequent periods throughout the snapshot. We define the number of sensing targets as n_s. If $n_s \leq T_{sensing}$, the scheduling process is straightforward, as it is easy to allocate the targets across TTIs such that at most one sensing task is scheduled per TTI. However, when $n_s > T_{sensing}$, multiple sensing tasks must be scheduled within the same TTI. In such cases, the sensing scheduling algorithm prioritizes co-scheduling of the sensing signals aimed at distinct targets within the same TTI that are positioned farthest from one another. This approach minimizes the likelihood of overlapping topologies, reducing the need for cells to spatially multiplex the sensing signals for such targets, thereby decreasing the probability of interference between sensing tasks. Figure 5.2 provides an example of sensing scheduling, where (i) and (ii) illustrate an instance of a sensing schedule when $n_s \leq T_{sensing}$, and $n_s > T_{sensing}$, respectively. As we can notice from Figure 5.2(ii), in this example the two pars of targets that are furthest away with respect to each other are (s_1, s_6) and (s_4, s_7).

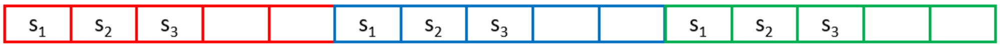

(i) Schedule for n_s sensing tasks where $n_s \leq T_{sensing}$.

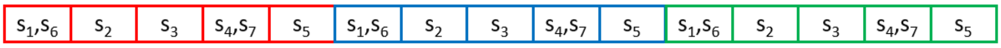

(ii) Scheduling of n_s sensing tasks where $n_s > T_{sensing}$.

Figure 5.2: Schedule for n_s sensing tasks when $T_{sensing} = 5\,TTIs$ and (i) $n_s \leq T_{sensing}$ and (ii) $n_s > T_{sensing}$.

5.5.2 Communication users scheduling

Conversely, communication user scheduling occurs at each TTI t. A commonly used scheduler in mobile networks is the Proportional Fairness (Proportional Fair (PF)) scheduler, which balances maximizing cell throughput with ensuring fairness among users [46]. The PF scheduler allocates resources to users based on the ratio between their estimated instantaneous data rate and their historical average experienced data rate. For a given user u, the PF index at TTI t is defined as:

$$PF_u(t) = \frac{\widetilde{R}_u(t)}{R_u^{\text{av}}(t-1)} \tag{5.5.1}$$

where $\widetilde{R}_u(t)$ is the estimated data rate for user u at TTI t, and $R_u^{\text{av}}(t-1)$ is the user's average throughput up to time $t-1$. The scheduler prioritizes users with the highest PF index for resource allocation in the upcoming TTI.

To implement multi-user scheduling, we combine the PF ranking of users with a decision criterion to determine which users can be scheduled simultaneously. In this work, we adopt a modified version of the Semi-Orthogonal User Selection (SUS) algorithm [47], as presented in [48]. This method ensures that users with approximately orthogonal channel vectors are co-scheduled, thereby reducing interference between them. We have slightly modified this algorithm to co-schedule users alongside the already co-scheduled signals for the sensing tasks, which occur at recurring TTIs.

Steps of the Semi-Orthogonal User Selection Algorithm:

1. **Step 1 (Initialization):**
   We define $\mathcal{E}_c^S(t)$ as the set of scheduled entities in the cell c at TTI t. If there are sensing tasks scheduled in cell c at the considered TTI t, we include them in $\mathcal{E}_c^S(t)$.

2. **Step 2 (Co-scheduling additional users):**
   Assume k entities are already scheduled. To co-schedule an additional user u, we select the user with the highest PF index as:

   $$u = \arg\max_{u \in \mathcal{U}_c} PF_u(t)$$

   where U_c is the set of users associated with cell c. Subsequently, we select the candidate user's channel vector $\mathbf{h}_u(t)$, which represents the channel between the cell c and user u's receiving antenna which experiences the highest gain. We compute the correlation between the candidate user's channel vector $\mathbf{h}_u(t)$ and the already scheduled users' channel vectors. For each candidate user u, calculate the orthogonality condition:

$$\gamma_u = \frac{|\mathbf{h}_u(t)^{\mathrm{H}}\mathbf{h}_{e_k}(t)|}{\|\mathbf{h}_u(t)\|_2\|\mathbf{h}_{e_k}(t)\|_2}$$

If $\gamma_u \leq \gamma_{th}$, where $\gamma_{th} = 0.5$ [47], the user u is considered sufficiently orthogonal to the already scheduled users and is added to the scheduling set:

$$\mathcal{E}_c^S = \mathcal{E}_c^S(t) \cup \{u\}$$

3. **Step 3 (Update and Repeat):**
   The process continues until no more users can be co-scheduled based on the orthogonality criterion. The final set $\mathcal{E}_c^S(t)$ contains the scheduled users for cell c at time t, ensuring minimal interference between them.

This approach results in a set of scheduled entities that are co-scheduled in such a way that their transmissions experience minimal interference, as their channel vectors are approximately orthogonal. The list of scheduled entities is then passed to the beamforming stage for precoder design.

Chapter 6

Scenarios and results

In this chapter, we present the results of our performance evaluation of a communication-centric JCAS network. The focus of the analysis is on assessing the trade-offs between communication and sensing performance. Specifically, we evaluate four Key Performance Indicators (KPIs): the average and 10^{th} percentile probability of detection for sensing tasks, and the average and 10^{th} percentile throughput for communication flows. Our findings highlight how varying system parameters influence these KPIs, providing insights into optimal configurations for balanced performance.

To conduct this evaluation, we examine the KPIs across a range of scenarios by varying key system parameters. The configurable parameters used in these scenarios are listed in Table 6.1, where the underlined values indicate the default settings, unless otherwise specified.

Table 6.1: Scenario parameters varied in the simulations.

Parameter	Symbol	Values	Units
Number of UEs per cell	n_{UE}	0, $\underline{1}$, 5	-
Number of targets	n_s	$\underline{1}$, 5, 10	-
Sensing topology selection parameter	G_{th}	0, 3, 6, 9, 12, 15	dB
Radar cross-section	RCS	$\underline{10}$, 50, 100	m^2
$I_{communication}$ weighting factor	β_c	0, 0.5, $\underline{1}$	-
$I_{sensing}$ weighting factor	β_s	0, 0.5, $\underline{1}$	-
Background cells activity factor	δ_p	0, $\underline{0.5}$, 1	-

The fixed parameters applied consistently throughout all simulations are provided in Table 6.2.

In the following subsections, we describe the scenarios considered in this study and present the corresponding simulation results.

6.1 Sensing-only scenario

In this section, we evaluate the sensing performance of the JCAS system in the absence of active communication flows. Under these conditions, all UEs are fully dedicated to sensing tasks, while the background cells remain silenced, meaning $\delta_p = 0$. The scenario under consideration involves five active sensing tasks, with a variable number of UEs per cell. Given the sensing periodicity of $T_{\text{sensing}} = 5$ TTIs, scheduling these five tasks does not necessitate spatial multiplexing of sensing signals. Our objective is to assess how variations in the number of UEs affect the probability of detection and to examine the influence of the sensing topology selection parameter G_{th} on both the topology size and sensing performance.

Table 6.2: Fixed parameters assumed in all scenarios.

Name	Symbol	Value	Unit
Inter-site distance	ISD	500	m
Numerology	-	1	-
Sub-carrier spacing	SCS	30	kHz
Carrier bandwidth	B	20	MHz
Number of PRBs	n_{PRB}	51	-
Frequency	f	7.1875	GHz
TTI duration	-	0.5	ms
BS antenna array	-	64T64R	-
UE antenna array	-	1T4R	-
UE/target speed	-	0.8	m/s
PF smoothing parameter	α	0.1	-
Co-scheduling parameter	γ	0.5	-
Probability of false alarm	P_{fa}	10^{-6}	-
UE antenna element gain	A_{UE}	0	dB
BS antenna element gain	A_{BS}	8	dB
Noise figure of a UE	NF_{UE}	8	dB
Noise figure of a BS	NF_{BS}	2	dB
Shadowing standard deviation	σ	6	dB
Shadowing correlation	ρ	0.5	-
BS height	h_{BS}	22.5	m
UE height	h_{UE}	1.5	m
Correction factor throughput	-	0.75	-
Sensing period	$T_{sensing}$	5	TTI

The results for this scenario are shown in Figure 6.1. In Figure 6.1(i), the solid lines illustrate the average *selected* topology size, while the dashed lines depict the average *effective* topology size for different numbers of UEs per cell. Figure 6.1(ii) shows the average probability of detection (solid lines) and the 10^{th} percentile probability of detection (dashed lines) as the number of UEs per cell varies.

From the solid curves in Figure 6.1(i), we observe that the average topology size increases with both G_{th} and the number of available UEs. This is expected, as a larger G_{th} allows the sensing topology selection algorithm to include more nodes in the topology, and with more UEs, it becomes more likely that several users will have a sufficiently good channel link to the target, making them eligible for inclusion in the sensing topology. Additionally, the average *effective* topology size is only marginally smaller than the average *selected* topology size, indicating that the dynamic node contribution management algorithm removes very few node contributions. This behavior is expected in a sensing-only scenario since, without interference, even nodes with weaker channels towards the target can still positively contribute to the detection task. It is also worth noting that, contrary to what might be expected, the curves are not zero when $G_{\text{th}} = 0\ dB$. This indicates that the average topology size, both *selected* and *effective*, is not strictly one. In scenarios with one or five UEs, if the strongest channel gain between the target and any candidate node belongs to a UE, the sensing topology selection algorithm selects a topology of size two, where the second node is the cell with the highest gain among all candidate cells. Naturally, for the case where there is only one UE per cell, this situation cannot occur, and the average topology size remains exactly one.

From Figure 6.1(ii), we observe that the probability of detection increases with the sensing topology selection parameter $G_{\text{th}} > 15.$, as the sensing topology expands with higher G_{th}. Additionally, we notice that both the curves of average and 10^{th} percentile probability of detection almost exactly match for the cases with zero or one UE per cell, while the case with five UEs per cell achieves significantly better performance. This is observed because a higher number of UEs per cell allows the sensing topology selection algorithm to select larger topologies and, the larger the number of UEs, the more likely it is for at least one UE to be close to the target, therefore probably experiencing a good channel towards the target.

Finally, the plots in Figure 6.1 indicate that for scenarios with zero and one UE per cell, the probability of detection converges around $G_{\text{th}} = 12$. In these cases, this corresponds to an average topology size of 1.5 and 2, respectively. However, in the case with five UEs per cell, the curves suggest that the probability of detection may continue to improve for $G_{\text{th}} > 15$.

Since the main objective of this thesis is to analyze the trade-off between communication and sensing in JCAS networks, and other sensing-only scenarios exhibit similar trends to those presented in this section, we choose to focus on the more insightful JCAS scenarios in the next section.

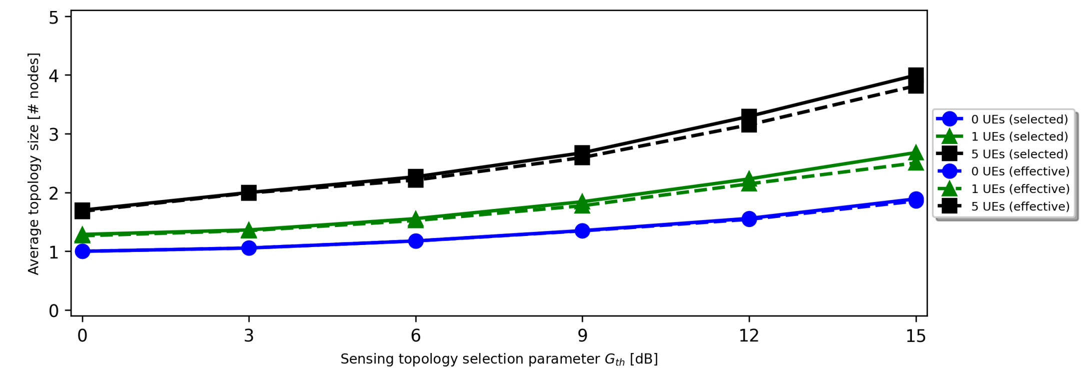

(i) Average topology size vs sensing topology selection parameter G_{th}

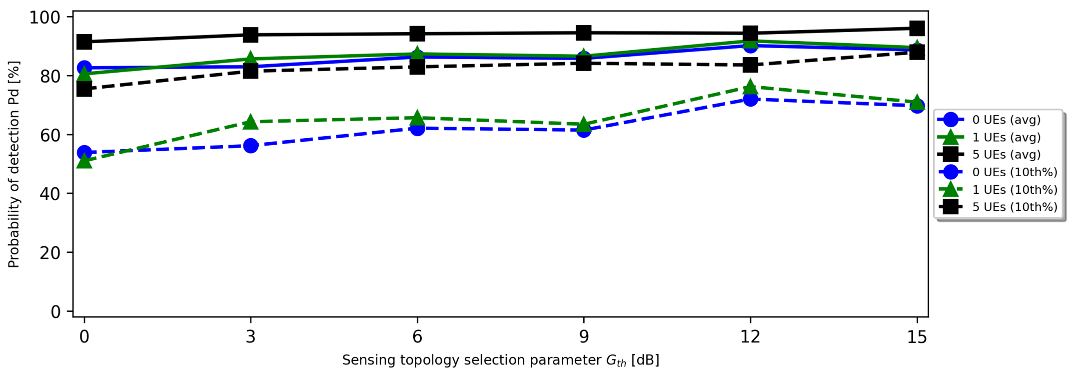

(ii) Probability of detection Pd vs sensing topology selection parameter G_{th}

Figure 6.1: Analysis of the impact of G_{th} on the probability of detection and sensing topology size in a sensing-only scenario with five active sensing tasks and different numbers of UEs per cell.

6.2 JCAS scenarios

This section analyzes the sensing performance of the JCAS system when both sensing tasks and communication flows are simultaneously active. In these scenarios, all UEs are available for selection in the sensing topology. If a UE u is selected to participate in the sensing topology for a sensing task s, it will not be scheduled for downlink data transfer during the TTIs when s is scheduled. However, the UE can still be scheduled for downlink data transfer in other TTIs. In these scenarios, all configurable parameters are set to their default values unless otherwise specified.

6.2.1 Performance impact of G_{th} given five sensing tasks and different number of UEs

In this scenario, we assess the influence of the sensing topology selection parameter G_{th} on the average and 10^{th} percentile probability of detection, the average and 10^{th} percentile user throughput, as well as the average *selected* and *effective* topology sizes. The evaluation is conducted with five active sensing tasks, comparing performance across different numbers of UEs per cell. The results are presented in Figure 6.2, where all three plots display outcomes as a function of G_{th}. Figure 6.2(i) shows the average *selected* topology size (solid lines) and the average *effective* topology size (dashed lines). Figure 6.2(ii) illustrates the average probability of detection (solid lines) and the 10^{th} percentile probability of detection (dashed lines). Finally, Figure 6.2(iii) presents the average (solid lines) and 10^{th} percentile (dashed lines) user throughput.

Figure 6.2(i) shows the impact of G_{th} on the sensing topology size, allowing for a comparison with the sensing-only scenario presented in Figure 6.1(i). From the solid curves, we observe that the average size of the sensing topologies selected by the sensing topology selection algorithm remains the same, as expected, since the *selected* topology is not influenced by interference. However, the *effective* average topology size tends to be smaller. This reduction reflects the fact that in the JCAS scenario, due to communication interference and the need to share the available resources with the UEs, fewer nodes in the sensing topology positively contribute to detection tasks. Consequently, the performance of sensing tasks is degraded compared to the sensing-only scenario. Notably, this effect is more pronounced in the case of five UEs per cell, where the larger number of UEs leads to greater communication interference and fewer resources allocated to sensing tasks. In contrast, the curve representing the case of no UEs is unaffected. Interestingly, having a greater number of UEs available for selection in the sensing topology does not necessarily translate into substantial improvements in sensing detection performance.

Figure 6.2(ii) shows an improvement in the average probability of detection as G_{th} increases, which corresponds to a larger average topology size. Interestingly, the curve representing one UE per cell exhibits a slightly higher average probability of detection compared to the curve for five UEs per cell. This outcome highlights a trade-off: while a larger sensing topology size increases the probability of detection, the additional interference introduced by more UEs participating in communication flows negatively impacts the sensing tasks. Overall, both the average and 10^{th} percentile probabilities of detection are notably lower than those observed in the sensing-only scenario. This reduction is attributed to the interference from communication flows and the resource sharing between sensing tasks and communication flows.

Figure 6.2(iii) presents the average and 10^{th} percentile user throughput for scenarios with one and five UEs per cell. As expected, the results indicate that when fewer UEs are present in the network, both the average and 10^{th} percentile user throughput are higher. This improvement is attributed to the fact that fewer UEs lead to more efficient resource allocation, as fewer resources are shared and less interference is generated. It is important to note that in this scenario, the average throughput remains unaffected by G_{th}, and consequently by the sensing topology size, while the 10^{th} percentile throughput is only marginally influenced. This outcome is supported by the fact that only one sensing task is scheduled per TTI, and the average sensing topology size is very small, as shown in Figure 6.2(i). As a result, very few communication flows are impacted by the sensing tasks, leaving the average user throughput largely unaffected. The 10^{th} percentile user throughput is impacted for UEs that are part of the sensing topology at a given TTI t. However, due to the use of a PF scheduler, these UEs are more likely to be scheduled in subsequent TTIs, compensating for the temporarily lost throughput performance. We can anticipate that the impact of sensing tasks on user throughput will increase as the number of active sensing tasks grows.

6.2.2 Performance impact of G_{th} given one UE per cell and different number of sensing tasks

In this scenario, we examine the impact of the sensing topology selection parameter G_{th} on both the average and 10^{th} percentile probability of detection, as well as on the average and 10^{th} percentile user throughput. The evaluation is conducted considering one active UE per cell, comparing performance across different numbers of sensing tasks. The results are presented in Figure 6.3.

Figure 6.3(i) shows the probability of detection as a function of the sensing topology selection parameter G_{th}. The one-target and five-target scenarios exhibit overlapping curves because, in the five-target scenario, each target is scheduled in a separate TTI, effectively preventing inter-task interference and resource sharing. In contrast, the ten-target scenario follows a similar trend but consistently shows lower performance due to increased inter-task interference and competition for resources among multiple sensing tasks, as the tasks are spatially multiplexed. These observations emphasize the impact of inter-task interference: while increasing G_{th} generally improves the probability of detection by expanding the sensing topology, the presence of multiple concurrent sensing tasks can cancel this gain through inter-task interference and resource sharing. The graph also shows that the 10^{th} percentile probability of detection for the scenario with ten sensing tasks drops to zero for low values of G_{th}. This occurs in cases where it is not possible to schedule sensing tasks within the same TTI that are sufficiently orthogonal, leading to a high level of inter-task interference, which significantly degrades sensing performance.

Figure 6.3(ii) shows that the average throughput is minimally affected by the number of active sensing tasks, with the curves for one, five, and ten targets remaining constant and closely aligned. This is expected, as mentioned in the previous scenario, because a small number of sensing tasks with a small average topology size do not significantly impact user throughput. However, the 10^{th} percentile communication throughput is more affected by the number of targets, as more sensing tasks involve a greater number of UEs in sensing activities, thereby reducing their availability for communication and impact their communication performance.

6.2.3 Impact of target distance on probability of detection

In this section, we present the results of a study analyzing the correlation between the distance from the target to the cell experiencing the highest gain and the average probability of detection. The scenario involves one target and different numbers of UEs per cell, evaluated for sensing topology selection parameters of $G_{\text{th}} = 3$ dB and $G_{\text{th}} = 15$ dB. The results are shown in Figure 6.4(i) and Figure 6.4(ii), respectively.

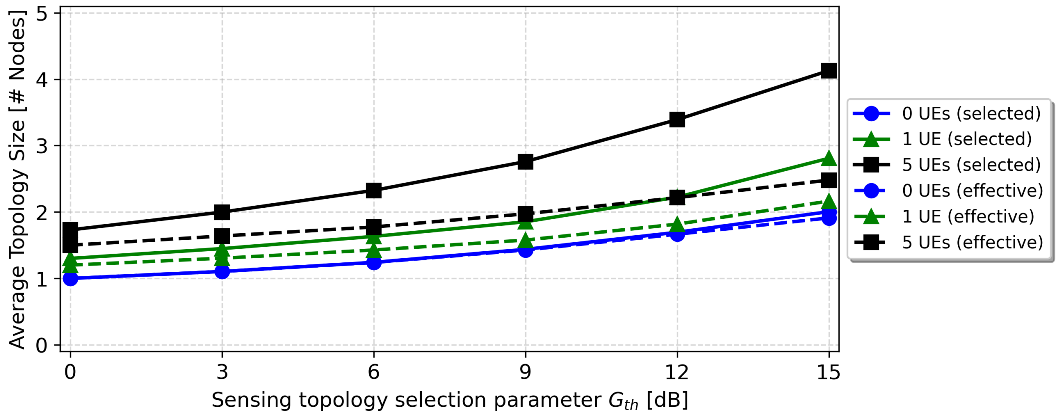

(i) Average Topology Size vs. Sensing Topology Selection Parameter G_{th}

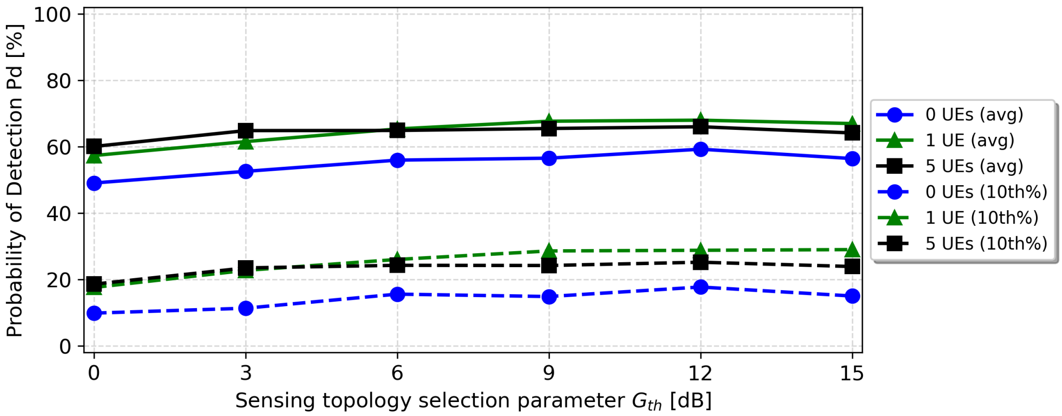

(ii) Probability of Detection Pd vs. Sensing Topology Selection Parameter G_{th}

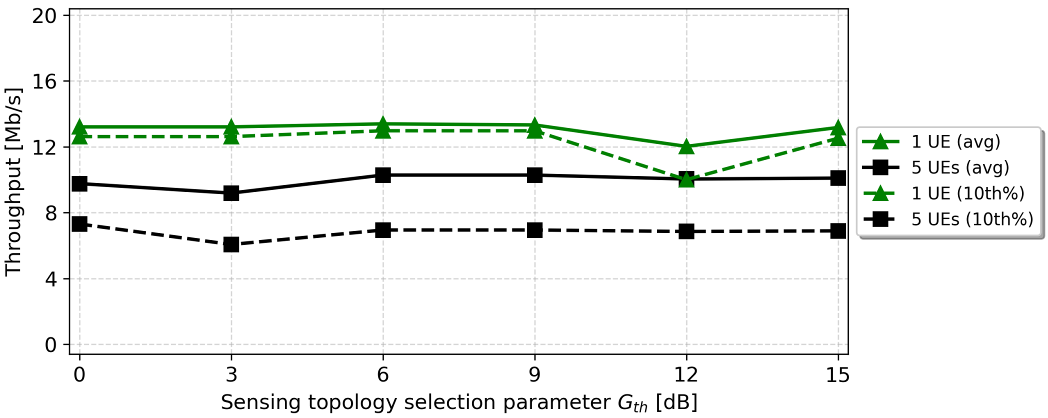

(iii) Throughput vs. Sensing Topology Selection Parameter G_{th}

Figure 6.2: Analysis of the impact of G_{th} on the probability of detection, communication throughput and sensing topology size in a JCAS scenario with five active sensing tasks and different numbers of UEs per cell.

From the figure, we observe a strong inverse relationship between the probability of detection and the distance from the target to the cell with the highest gain, which is in line with an exponential path-loss model. Additionally, it is noteworthy that for larger distances, the scenario with $G_{\mathrm{th}} = 15$ dB tends to outperform the scenario with $G_{\mathrm{th}} = 3$ dB. This confirms that a larger topology size, as determined by

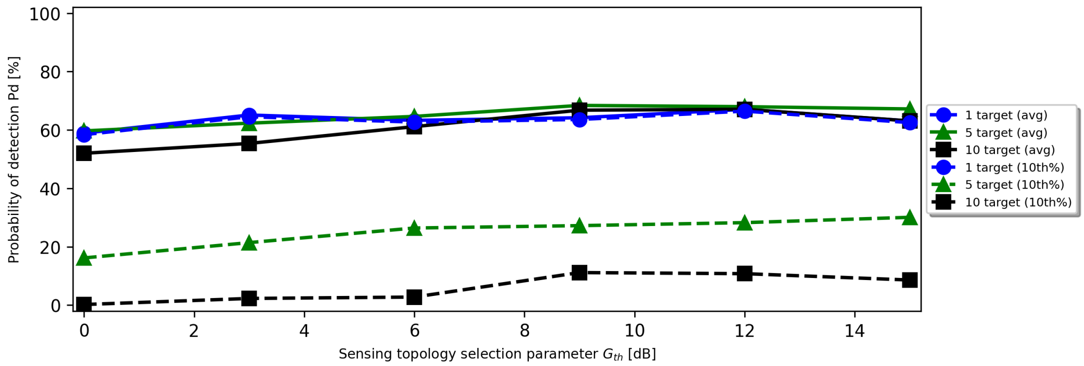

(i) Probability of detection Pd vs sensing topology selection parameter G_{th}

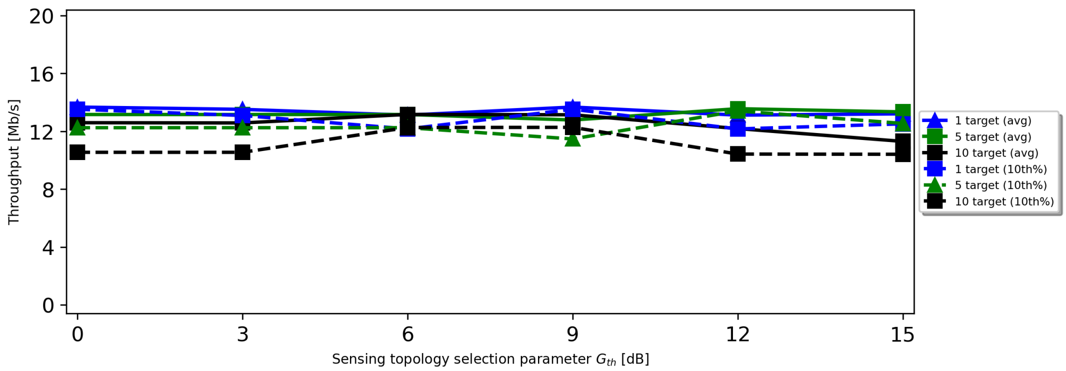

(ii) Throughput vs sensing topology selection parameter G_{th}

Figure 6.3: Analysis of the impact of G_{th} on the probability of detection and communication throughput in a JCAS scenario with one UE per cell and different number of active sensing tasks.

a higher G_{th}, achieves higher sensing performance by effectively enhancing the detection probability at greater distances.

Lastly, we observe that for lower values of G_{th}, the three curves exhibit very similar levels of sensing performance, suggesting that the contribution of the cell experiencing the highest gain in the sensing topology accounts for most of the sensing performance. As G_{th} increases, this contribution diminishes, and the cases with one and five UEs per cell begin to show improved sensing performance with respect to the case with no UEs per cell. The plots also highlights the trade-off between the number of UEs per cell and sensing performance, which was similarly observed in Figure 6.2(ii), where the curve for one UE per cell outperforms the one for five UEs per cell.

6.2.4 Impact of RCS on probability of detection

In this section, we examine how different RCS values affect the probability of detection in a scenario with five active sensing tasks and one UE per cell, considering different G_{th} values. As intuitively expected, Figure 6.5(i) shows that the probability of detection increases with RCS, due to the fact that a bigger sensing object generally reflects more energy in the receiver direction. The improvement is more pronounced when comparing 10 m^2 and 50 m^2 than 50 m^2 and 100 m^2. This trend occurs because RCS impacts the SINR linearly, as described in Equation 4.2.3, while the probability of detection grows logarithmically with SINR, as shown in Figure 4.4.

Throughput performance is included in Figure 6.5(ii) for completeness, although it is intuitively clear

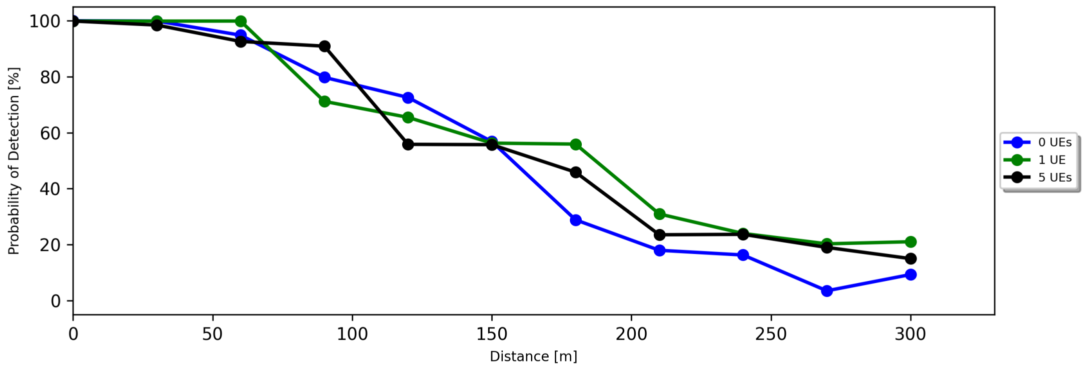

(i) Probability of Detection vs Distance for $G_{th} = 3dB$

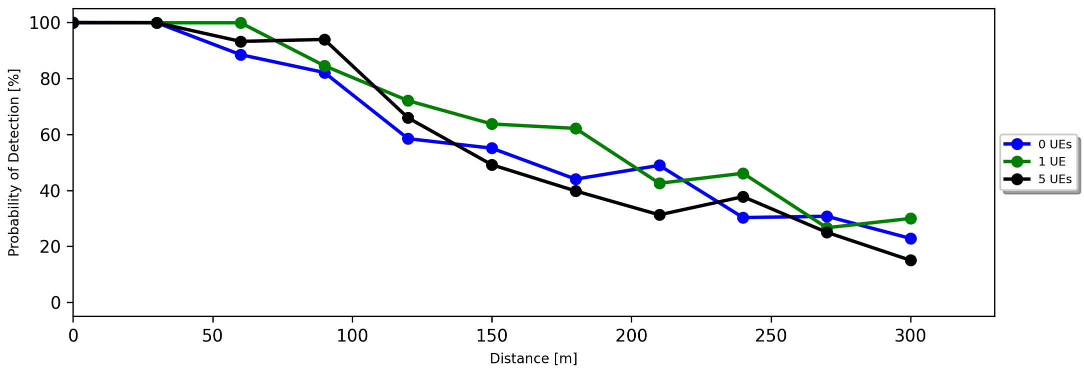

(ii) Probability of Detection vs Distance for for $G_{th} = 15dB$

Figure 6.4: Analysis of the impact of the distance between the target and the cell with strongest channel on the probability of detection in a JCAS scenario with one active sensing tasks and different numbers of UEs per cell for $G_{\mathrm{th}} = 3\ dB$ and $G_{\mathrm{th}} = 15\ dB$.

that the RCS primarily affects sensing performance and does not directly impact user throughput. In practice, the sensing performance gains under higher RCS values could be (partially) traded off to improve throughput performance by reducing the sensing topology size, which would in turn reduce interference and potentially allow more transmission opportunities for UEs. However, for the current scenarios, this gain would be minimal.

6.2.5 Impact of δ_p on the probability of detection

In this section, we examine the effect of different values of the background cells' activity factor δ_p on the probability of detection in a scenario with five active sensing tasks and one UE per cell, across various values of G_{th}. The results, shown in Figure 6.6, clearly demonstrate the expected impact of interference from the background cells on detection performance. This influence is evident in both the average and 10^{th} percentile probabilities of detection, highlighting how increased interference degrades sensing performance.

6.2.6 Impact of β_c and β_s on the probability of detection

In this section, we analyze the effect of different values of the weighing factor for the communication interference β_c and the weighting factor for the sensing interference β_s on the probability of detection in a scenario with ten active sensing tasks and one UE per cell, while considering different values of G_{th}. Specifically, we investigate the average probability of detection for all possible combinations of β_c and β_s. The scenario includes ten active sensing tasks, as opposed to five sensing tasks assumed in previous

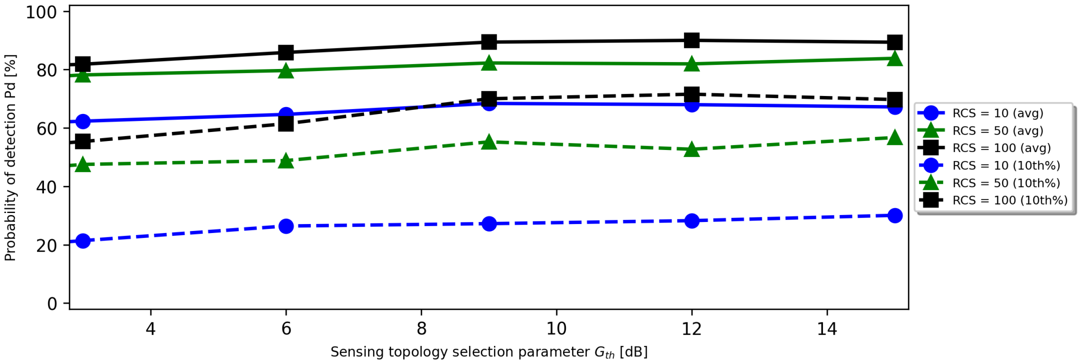

(i) Probability of detection Pd vs sensing topology selection parameter G_{th}

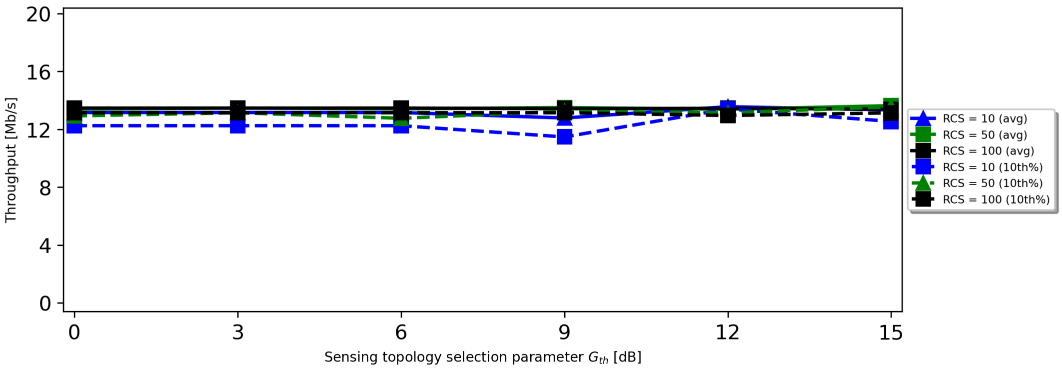

(ii) Throughput vs sensing topology selection parameter G_{th}

Figure 6.5: Analysis of the impact of the RCS on the probability of detection and communication throughput in a JCAS scenario with five active sensing tasks and different numbers of UEs and G_{th}.

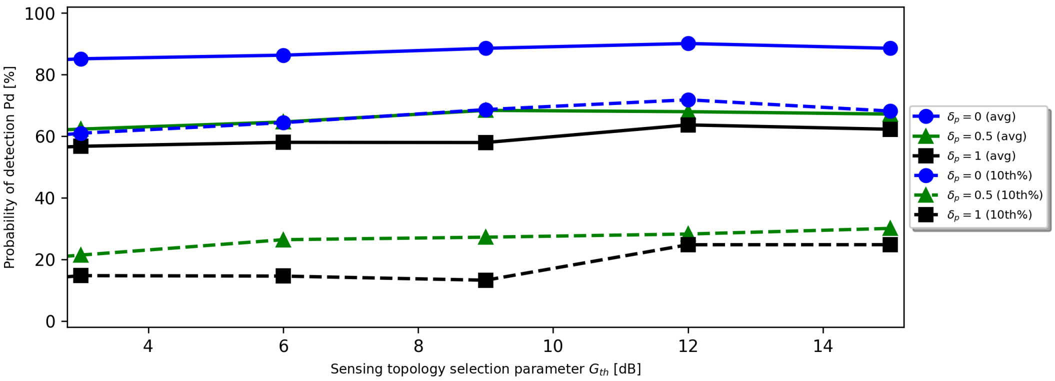

(i) Probability of detection Pd vs sensing topology selection parameter G_{th}

Figure 6.6: Analysis of the impact of the δ_p on the probability of detection in function of G_{th} in a JCAS scenario with five active sensing tasks and one UE per cell.

scenarios, because β_s regulates the interference contribution from one sensing task to another. In cases where there are at most five active sensing tasks, no such interference occurs, because the associated sensing signals are transmitted in distinct TTIs, making it uninformative to study the impact of β_s. The results of this analysis are presented in Figure 6.7. As shown in the figure, the average probability of detection is only marginally affected by different values of β_c and β_s.

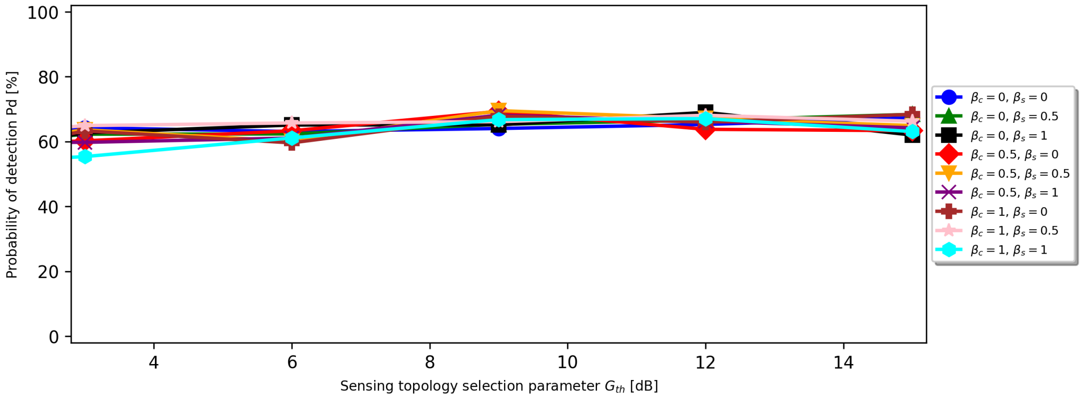

(i) Probability of detection Pd vs sensing topology selection parameter G_{th}

Figure 6.7: Analysis of the impact of the β_c and β_s on the probability of detection in a JCAS scenario with ten active sensing tasks and one UE per cell.

Chapter 7

Conclusions and future work

In this thesis, we developed a model for communication-centric JCAS networks and proposed novel RRM algorithms to optimize the trade-off between communication and sensing performance. Specifically, we introduced a sensing topology management algorithm aimed at maximizing target detection probability which, in the analysed scenarios, only minimally impacts the user throughput. By adjusting key model parameters, we evaluated the performance of these algorithms in terms of probability of detection and user throughput across diverse scenarios.

7.1 Summary of the findings

This section presents the key insights from evaluating the proposed JCAS network, focusing on the trade-off between communication and sensing. Based on the considered scenarios, the main findings are:

1. **Trade-off between the number of UEs and sensing performance:** Increasing the number of UEs in JCAS networks, where UEs are engaged in active communication flows and can also participate in sensing topologies, improves detection probability by enlarging the sensing topologies, but it also increases communication interference that impacts sensing tasks. Our results show that, in the scenarios analyzed in this thesis, there is a number of UEs to guarantee optimal sensing performance. In fact, scenarios with one UE per cell outperform those with five UEs, suggesting that fewer UEs per cell achieve better detection performance while minimizing interference. These findings can be applied to real-world scenarios where operators may have control over which UEs are active in communication flows and which UEs can contribute to sensing, based on their subscription type. In fact, operators could adjust scheduling parameters based on subscription priorities, favoring users with higher-priority subscriptions and allocating fewer resources to users with basic plans, if the number of co-scheduled UEs exceeds the optimal level, in order to maintain good sensing performance.

2. **Impact of G_{th} on the sensing and communication performance:** Increasing the sensing topology parameter G_{th} positively impacts the probability of detection, as it results in employing larger sensing topologies. In the specific scenarios studied in this thesis, the impact of G_{th} on communication performance is marginal. However, in scenarios with more active sensing tasks, the impact on communication performance would likely be more significant.

7.2 Future work

Several potential directions for future work have emerged from this research. Key areas that could be explored include:

1. Extending the model to consider different types of sensing tasks (e.g., localization, surveillance, and tracking) and their impact on communication, as well as considering moving targets instead of static, locally moving targets.
2. Developing adaptive algorithms that dynamically adjust system parameters in real-time to balance the trade-off between communication and sensing, such as periodically selecting updated sensing topologies by considering the average historical level of experienced interference.
3. The current RRM algorithms assume perfect CSI. Investigating the impact of imperfect CSI and developing efficient CSI acquisition methods to support radio resource management tasks are promising directions for future research.
4. Exploring the integration of ML/AI techniques to enhance the performance and computational feasibility of RRM algorithms. For instance, incorporating an AI model that can predict interference levels at upcoming TTIs and optimally allocate resources based on these predictions.

Bibliography

[1] A. Zhang, M. L. Rahman, X. Huang, Y. J. Guo, S. Chen, and R. W. Heath, "Perceptive Mobile Networks: Cellular Networks with Radio Vision via Joint Communication and Radar Sensing," *IEEE Vehicular Technology Magazine*, vol. 16, no. 2, pp. 20–30, Dec. 2021.

[2] F. Dong, F. Liu, Y. Cui, W. Wang, K. Han, and Z. Wang, "Sensing as a Service in 6G Perceptive Networks: A Unified Framework for ISAC Resource Allocation," *IEEE Transactions on Wireless Communications*, vol. 22, no. 5, pp. 3522–3536, 2023.

[3] P. Kumari, J. Choi, N. González-Prelcic, and R. W. Heath, "IEEE 802.11ad-based radar: An approach to joint vehicular communication-radar system," *IEEE Trans. Veh. Technol.*, vol. 67, no. 4, pp. 3012–3027, Apr. 2018.

[4] C. Sturm and W. Wiesbeck, "Waveform design and signal processing aspects for fusion of wireless communications and radar sensing," *Proc. IEEE*, vol. 99, no. 7, pp. 1236–1259, Jul. 2011.

[5] D. Ma, N. Shlezinger, T. Huang, Y. Liu, and Y. C. Eldar, "Joint radar-communication strategies for autonomous vehicles: Combining two key automotive technologies," *IEEE Signal Process. Mag.*, vol. 37, no. 4, pp. 85–97, Jul. 2020.

[6] J. A. Zhang, M. L. Rahman, K. Wu, *et al.*, "Enabling Joint Communication and Radar Sensing in Mobile Networks—A Survey," *IEEE Communications Surveys & Tutorials*, vol. 24, no. 1, pp. 306–345, 2022.

[7] F. Liu, L. Zheng, Y. Cui, *et al.*, "Seventy Years of Radar and Communications: The Road from Separation to Integration," *IEEE Signal Processing Magazine*, vol. 40, no. 5, pp. 106–121, 2023.

[8] F. Liu, W. Yuan, X. Zhou, X. Duan, J. Lian, *et al.*, "Integrated sensing and communications: Recent advances and ten open challenges," *arXiv preprint arXiv:2305.00179*, 2023. [Online]. Available: https://arxiv.org/abs/2305.00179.

[9] C. B. Barneto, T. Riihonen, S. D. Liyanaarachchi, M. Heino, N. González-Prelcic, and M. Valkama, "Beamformer Design and Optimization for Full-Duplex Joint Communication and Sensing at mm-Waves," *IEEE Transactions on Communications*, 2021.

[10] Y. Yao, H. Zhou, and M. E. Kantarci, "Joint Sensing and Communications for Deep Reinforcement Learning-Based Beam Management in 6G," *IEEE Transactions on Communications*, 2022.

[11] Y. Zhang, Q. Li, J. Wang, J. Wang, J. Chen, and Z. Han, "Toward Throughput Maximization of Integrated Sensing and Communications Enabled Predictive Beamforming for 6G," *IEEE Network*, 2023.

[12] D. N. Dao, H. Zhang, A. B. J. Kokkeler, and Y. Miao, "Joint Beamforming Optimization for Multi-user Multi-target FD JCAS System: A Hybrid GRQ-GA Approach," *arXiv preprint*, 2024.

[13] Y. Zeng, Y. Ma, and S. Sun, "Joint Radar-Communication with Cyclic Prefixed Single Carrier Waveforms," *IEEE Transactions on Vehicular Technology*, 2020.

[14] Z. Ni, J. A. Zhang, K. Yang, X. Huang, and T. A. Tsiftsis, "Multi-Metric Waveform Optimization for Multiple-Input Single-Output Joint Communication and Radar Sensing," *IEEE Transactions on Communications*, 2022.

[15] A. M. Abouelmaati, S. Aboagye, and H. Tabassum, "Joint Spectrum Partitioning and Power Allocation for Energy Efficient Semi-Integrated Sensing and Communications," *arXiv preprint*, 2024. arXiv: 2404.18187 [cs.IT].

[16] Z. Wei, S. Li, W. Yuan, R. Schober, and G. Caire, "Resource Allocation for OTFS-Based ISAC Systems," *IEEE Transactions on Communications*, vol. 71, no. 3, pp. 1324–1340, 2023.

[17] D. Xu, X. Yu, D. W. K. Ng, A. Schmeink, and R. Schober, "Robust and secure resource allocation for isac systems: A novel optimization framework for variable-length snapshots," *IEEE Transactions on Communications*, vol. 70, no. 12, pp. 8196–8214, 2022.

[18] J. Zhang, Z. Fei, X. Wang, P. Liu, J. Huang, and Z. Zheng, “Joint Resource Allocation and User Association for Multi-Cell Integrated Sensing and Communication Systems,” *EURASIP Journal on Wireless Communications and Networking*, 2013.

[19] M. R. Figueroa, P. K. Bishoyi, and M. Petrova, “Power Allocation Scheme for Device-Free Localization in 6G ISAC Networks,” *EURASIP Journal on Wireless Communications and Networking*, 2023.

[20] F. Dong, F. Liu, Y. Cui, W. Wang, K. Han, and Z. Wang, “Sensing as a service in 6g perceptive networks: A unified framework for isac resource allocation,” *IEEE Transactions on Wireless Communications*, vol. 22, no. 5, pp. 3522–3536, 2023.

[21] C. Kumar, S. Solanki, E. Lagunas, J. Querol, S. Chatzinotas, and B. Ottersten, “Full Duplex Joint Communications and Sensing for 6G: Opportunities and Challenges,” *arXiv preprint*, Aug. 2023.

[22] Z. Wei, W. Jiang, Z. Feng, *et al.*, “Integrated Sensing and Communication Enabled Multiple Base Stations Cooperative Sensing Towards 6G,” *arXiv preprint*, 2023. arXiv: 2310.07180 [cs.NI].

[23] K. Meng, C. Masouros, G. Chen, and F. Liu, “Network-Level Integrated Sensing and Communication: Interference Management and BS Coordination Using Stochastic Geometry,” *arXiv preprint*, 2023. arXiv: 2311.09052 [cs.IT].

[24] K. Meng, C. Masouros, G. Chen, and F. Liu, “BS Coordination Optimization in Integrated Sensing and Communication: A Stochastic Geometric View,” *arXiv preprint*, 2024. arXiv: 2401.04918 [cs.IT].

[25] K. Meng and C. Masouros, “Cooperative Sensing and Communication for ISAC Networks: Performance Analysis and Optimization,” *arXiv preprint*, 2024. arXiv: 2403.20228 [cs.IT].

[26] K. Meng, C. Masouros, A. P. Petropulu, and L. Hanzo, “Cooperative ISAC Networks: Performance Analysis, Scaling Laws and Optimization,” *IEEE Transactions on Communications*, 2024.

[27] N. Babu, C. Masouros, C. B. Papadias, and Y. C. Eldar, “Precoding for Multi-Cell ISAC: From Coordinated Beamforming to Coordinated Multipoint and Bi-Static Sensing,” *IEEE Transactions on Communications*, 2024.

[28] H. Zhu, A. Venus, E. Leitinger, S. Tertinek, and K. Witrisal, “Fusion of Active and Passive Measurements for Robust and Scalable Positioning,” *arXiv preprint*, 2024. arXiv: 2403.16150 [eess.SP].

[29] S. Agarwal, R. Litjens, G. Joseph, and K. Das, “Development and Assessment of Resource Management Solutions for Throughput Enhancement in a RIS-aided Mobile Network,” M.S. thesis, Delft University of Technology, 2023. [Online]. Available: https://repository.tudelft.nl/islandora/object/uuid%3Ad828746f-cdf5-4053-b7ac-fa7fd11fd4fb.

[30] 3GPP Technical Specification Group Radio Access Network, “Study on Channel Model for Frequencies from 0.5 to 100 GHz,” 3GPP, Technical Report TR38.901, 2019.

[31] 3GPP Technical Specification Group Radio Access Network, “Technical Specification Group Radio Access Network; User Equipment (UE) radio transmission and reception; Part 1: Introduction and Overview,” 3GPP, Technical Report TR38.101, 2020.

[32] F. Gunnarsson, M. N. Johansson, A. Furuskar, *et al.*, “Downtilted base station antennas - a simulation model proposal and impact on hspa and lte performance,” in *2008 IEEE 68th Vehicular Technology Conference*, 2008.

[33] H.-J. Li and Y.-W. Kiang, “10 - radar and inverse scattering,” in *The Electrical Engineering Handbook*, W.-K. Chen, Ed., Burlington: Academic Press, 2005, pp. 671–690, ISBN: 978-0-12-170960-0. DOI: https://doi.org/10.1016/B978-012170960-0/50047-5. [Online]. Available: https://www.sciencedirect.com/science/article/pii/B9780121709600500475.

[34] ETSI, “LTE; Evolved Universal Terrestrial Radio Access (E-UTRA); Radio Frequency (RF) System Scenarios (3GPP TR 36.942 Version 8.2.0 Release 8),” European Telecommunications Standards Institute (ETSI), Sophia Antipolis Cedex, France, Tech. Rep., Jul. 2009, Version 8.2.0, Release 8.

[35] R. Fraile, J. F. Monserrat, J. Gozálvez, and N. Cardona, “Mobile Radio Bi-Dimensional Large-Scale Fading Modelling with Site-to-Site Cross-Correlation,” *European Transactions on Telecommunications*, vol. 19, no. 1, 2008.

[36] S. Jaeckel, L. Raschkowski, K. Börner, L. Thiele, F. Burkhardt, and E. Eberlein, “QuaDRiGa - Quasi Deterministic Radio Channel Generator, User Manual and Documentation,” Fraunhofer Heinrich Hertz Institute, Technical Report, version v1.2.3-307, 2014.

[37] K. Brueninghaus, D. Astely, T. Salzer, *et al.*, "Link Performance Models for System Level Simulations of Broadband Radio Access Systems," in *2005 IEEE 16th International Symposium on Personal, Indoor and Mobile Radio Communications*, vol. 4, 2005.

[38] 3GPP, "NR; Physical Layer Procedures for Data," 3GPP Technical Specification Group Radio Access Network, Technical Report TS38.214, 2023.

[39] P. Mogensen, W. Na, I. Z. Kovacs, *et al.*, "LTE Capacity Compared to the Shannon Bound," in *2007 IEEE 65th Vehicular Technology Conference*, 2007.

[40] M. I. Skolnik, *Introduction to Radar Systems*, 2nd. McGraw-Hill, 1980.

[41] H. T. Friis, "A Note on a Simple Transmission Formula," *Proceedings of the IRE*, vol. 34, no. 5, pp. 254–256, 1946. DOI: 10.1109/JRPROC.1946.234568.

[42] M. A. Richards, J. A. Scheer, and W. A. Holm, *Principles of Modern Radar: Basic Principles*. SciTech Publishing, 2010.

[43] G. Brooker, *Introduction to Sensors for Ranging and Imaging* (Radar, Sonar, and Navigation). Institution of Engineering and Technology, 2009. [Online]. Available: https://digital-library.theiet.org/content/books/ra/sbra014e.

[44] 3rd Generation Partnership Project (3GPP), *NR; User Equipment (UE) procedures in idle mode and in RRC inactive state (Release 16)*, Version 16.1.0, Jul. 2020. [Online]. Available: https://www.3gpp.org/DynaReport/38304.htm.

[45] T. Yoo and A. Goldsmith, "On the optimality of multiantenna broadcast scheduling using zero-forcing beamforming," *IEEE Journal on Selected Areas in Communications*, vol. 24, no. 3, pp. 528–541, 2006. DOI: 10.1109/JSAC.2005.862421.

[46] D. Tse, M. K. T. Toh, and C. H. Hsu, "Dynamic proportional fair scheduling for multi-user mimo systems," *IEEE Transactions on Information Theory*, vol. 50, no. 4, pp. 675–690, 2004. DOI: 10.1109/TIT.2004.825682.

[47] T. Yoo and A. Goldsmith, "On the Optimality of Multiantenna Broadcast Scheduling Using Zero-Forcing Beamforming," *IEEE Journal on Selected Areas in Communications*, vol. 24, no. 3, 2006.

[48] S. Braam, R. Litjens, P. Smulders, and W. IJntema, "Assessment of distributed multi-user mimo transmission in 5g networks," in *Proceedings of the 18th ACM International Symposium on Mobility Management and Wireless Access*, 2020, pp. 125–132. DOI: 10.1145/3416012.3424629.